Physical Characterization of Early Galaxies in the Webb's First Deep Field SMACS J0723.3-7323

T. Morishita[1] and M. Stiavelli[2]
[1] IPAC, California Institute of Technology, MC 314-6, 1200 E. California Boulevard, Pasadena, CA 91125, USA
[2] Space Telescope Science Institute, 3700 San Martin Drive, Baltimore, MD 21218, USA
Received 2022 July 23; revised 2023 February 17; accepted 2023 February 23; published 2023 March 29

Abstract

This paper highlights initial photometric analyses of JWST NIRCam imaging data in the sightline of SMACS0723, aiming to identify galaxies at redshift $z > 7$. By applying a conservative Lyman-break selection followed by photometric-redshift analysis and visual inspection, we identify four F090W-dropout and two F150W-dropout sources, three of which were recently confirmed in an independent spectroscopic analysis to $z = 7.663$, 7.665, and 8.499. We then supplement our sample with a photometric-redshift selection, and identify five additional candidates at $7 < z_{\rm phot} < 13$. The NIRCam images clearly resolve all sources and reveal their subgalactic components that were not resolved/detected in the previous imaging by Hubble Space Telescope. Our spectral energy distribution analysis reveals that the selected galaxies are characterized by young stellar populations (median age of ~ 50 Myr) of subsolar metallicity ($\sim 0.2\,Z_\odot$) and little dust attenuation ($A_V \sim 0.5$). In several cases, we observe extreme Hβ+[O III] lines being captured in the F444W band and seen as color excess, which is consistent with their observed high star formation rate surface density. Eight of the 11 sources identified in this study appear in at least one of the recent studies (Adams et al.; Atek et al.; Donnan et al.; Harikane et al.; Yan et al.) of the same fields, implying the high fidelity of our selection. We crossmatch all high-z galaxy candidates presented in the five studies with our catalog and discuss the possible causes of discrepancy in the final lists.

Unified Astronomy Thesaurus concepts: Galaxy evolution (594); Lyman-break galaxies (979); Starburst galaxies (1570)

1. Introduction

Our exploration of galaxies in the early universe has been enabled by the Hubble Space Telescope (HST). Since the installation of Wide Field Camera 3 (WFC3), our redshift limit has been pushed toward $z \gtrsim 6$, the era known as the epoch of reionization (Gunn & Peterson 1965; Madau et al. 1999; Robertson et al. 2015). A tremendous amount of effort has been invested in the photometric search of early galaxies via Lyman-break technique (Steidel et al. 1996), revealing hundreds of galaxy candidates from various HST surveys (e.g., Bradley et al. 2012; Bouwens et al. 2015; McLeod et al. 2015; Oesch et al. 2018; Bowler et al. 2020). Spectroscopic follow-ups then have successfully confirmed ~ 20 of those candidates at $z > 7$ (e.g., Vanzella et al. 2011; Shibuya et al. 2012; Finkelstein et al. 2013; Oesch et al. 2015; Stark et al. 2015; Hashimoto et al. 2018; Roberts-Borsani et al. 2022b) up to ~ 12 (Oesch et al. 2016; Jiang et al. 2021).

The James Webb Space Telescope (JWST) has started revolutionizing our understanding of galaxies and stellar populations in the era. With its exquisite sensitivity coverage up to $\sim 5\,\mu$m, Near-Infrared Camera (NIRCam) plays the key role in pushing the redshift front of galaxy search, which enables the identification of sources beyond the previous limit (Naidu et al. 2022b; Castellano et al. 2022; Finkelstein et al. 2022) up to $z \gtrsim 20$. Identification of sources at such high redshifts is crucial to our understanding of the formation

of the first galaxies and stars (Stiavelli & Trenti 2010; Harikane et al. 2022; Pacucci et al. 2022).

As part of the Early Release Observations (ERO; Pontoppidan et al. 2022), JWST pointed to a field of SMACS0723, a massive galaxy cluster at $z = 0.390$, dubbed as the Webb's First Deep Field. This observing program, by utilizing all four instruments on board, provides a new glimpse of the universe. The new imaging data revealed a number of potentially interesting high-redshift sources both in the cluster center and parallel fields (Figure 1). Here we present our initial identification of galaxy candidates identified by Lyman-break dropout selection at $z > 7$. The simultaneous imaging of the NIRCam's dual modules allows us to explore early galaxies to (i) search for intrinsically faint but strongly magnified sources by gravitational lensing, and (ii) provides a reference to the cluster field, as well as a glimpse of galaxy search with JWST in normal fields. This paper is structured as follows: in Section 2, we present our analyses on the ERO data, including initial reduction and additional photometric flux calibration. We present our selection of high-z sources in Section 3 and analyses of their physical properties in Section 4. In Section 5, we estimate the number density of the final candidates and discuss the fidelity of those sources by comparing identified high-z sources in the same filed by other studies. Lastly, we discuss future prospects and provide the summary of this study in Section 6. Throughout, we adopt the AB magnitude system (Oke & Gunn 1983; Fukugita et al. 1996), cosmological parameters of $\Omega_m = 0.3$, $\Omega_\Lambda = 0.7$, $H_0 = 70\,{\rm km s}^{-1}\,{\rm Mpc}^{-1}$, and the Chabrier (2003) initial mass function.
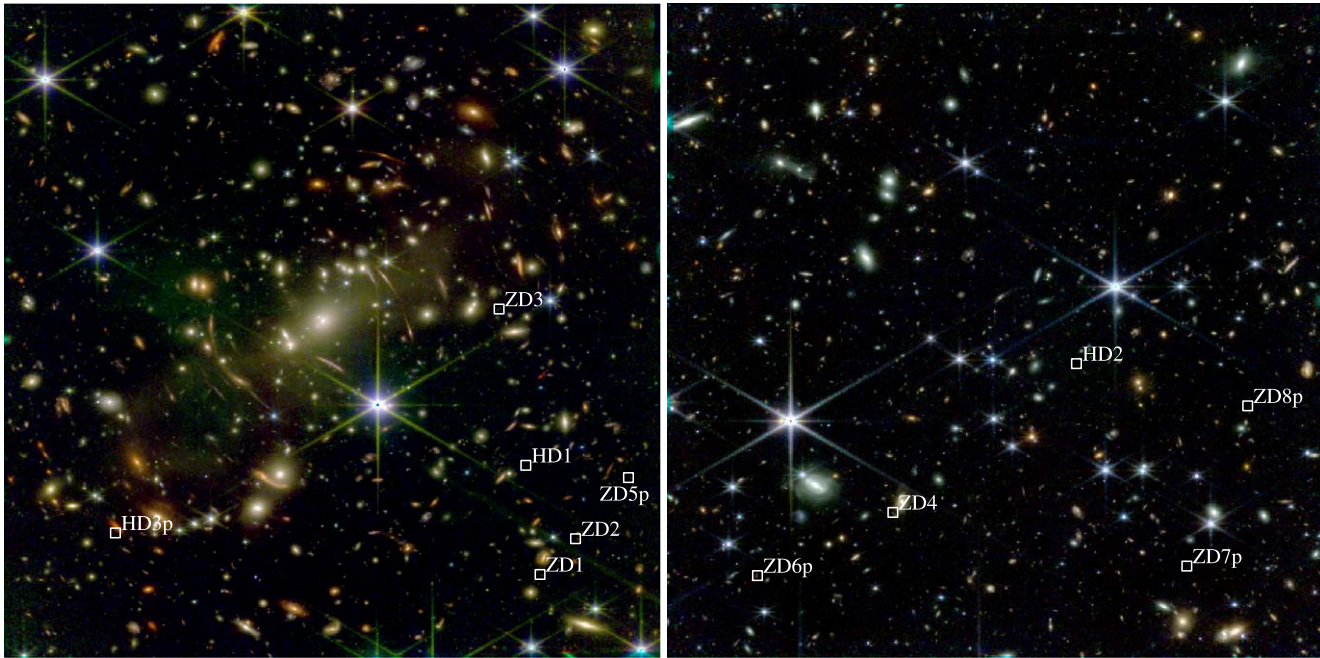
Figure 1. Left: composite RGB image of the Webb's First Deep Field, in the sightline of SMACS0723 (cluster field). The JWST NIRCam and NIRISS, and HST ACS and WFC3-IR images are combined (blue: F435W+F606W+F814W+F090W+F105W+F115W, green: F125W+F140W+F150W+F160W+F200W, red: F277W +F356W+F444W). The locations of the final high-z galaxy candidates (Section 4.1) are marked. Right: same but for the parallel field (blue: F090W+F150W, green: F200W+F277W, red: F356W+F444W).

2. Data and Analyses

2.1. JWST Early Release Observations Program

We focus our primary analysis on the NIRCam data taken as part of the JWST Early Release Observations Program, in the sightline of SMACS0723. The NIRCam imaging data consist of F090/150/200/277/356/444W filters, with ∼2 hr exposure on each. We also include Near Infrared Imager and Slitless Spectrograph (NIRISS) imaging data (F115W and F200W), taken as part of the wide slitless spectroscopic observation in the cluster field.

We retrieve raw data (_uncal.fits) from a dedicated AWS storage[3] placed by the MAST team at STScI. We reduce raw images by using the official pipeline (ver.1.7.2 along with the reference file context of jwst_0988.pmap) for detector calibration (DETECTOR) and photometric calibration (IMAGE STEP2), and then combine those in a common pixel grid (IMAGE STEP3).

We made a few changes to the default pipeline processes. First, we replaced the flat-field reference files for NIRCam images with those processed and published by Brammer (2022; NIRCAM Skyflats from grizli-v2). We find that those new flats, created with in-flight data, improve removing artifacts in the reduced images. We also adopt the magnitude zero points for NIRCam published by the same author.[4] While the latest version of the official reference files includes a similarly improved set of magnitude zero points (Boyer et al. 2022), our choice of adopting those by Brammer (2022) was made for the consistency with the flat files adopted above, though the difference is small (∼ a few percent) across the filters between the two studies. Lastly, during STEP2 and STEP3, we include

an extra step to subtract $1/f$-noise in _cal.fits images by using bbpn,[5] which follows the procedure presented in Schlawin et al. (2021). The final pixel scale is set to 0″0315.

Images are aligned to the common astrometric World Coordinate System (WCS) in multiple steps. First, we align the single F444W image to the GAIA-DR3 WCS frame. The rest of the NIRCam images and the NIRISS images are then aligned to the F444W image, by using both point sources and compact galaxies. We refine the pixel grid of all images to the one of F444W reproject.[6]

To homogenize the point-spread function (PSF) of the NIRCam and NIRISS images to the one of F444W, we generate convolution kernels by following the same procedure in Morishita (2021). Bright stars are identified by cross-matching our sources with the GAIR DR3 catalog. We visually inspect each of them and exclude those saturated or contaminated by neighboring objects. We then resample each PSF to align those at a subpixel level and stacked stars of each filter to generate a median PSF. We then provide the median-stacked stars to pypher (Boucaud et al. 2016) and generate convolution kernels for each filter. The quality of convolved PSFs is excellent, with ≪1% agreement in the encircled flux at radius $r = 0″16$, within which our photometric fluxes are extracted.

We also include the HST data available in the cluster field, originally taken in the RELICS program (Coe et al. 2019; Salmon et al. 2020), to supplement our selection. We retrieve raw data from MAST, which consist of seven filters (F435/606/814/105/125/140/160W) and reduce those by using borgpipe (Morishita 2021). It is noted that the HST coverage is only for the cluster field. For the HST images, we repeat a similar analysis as for NIRCam, but convolve

---

[3] https://outerspace.stsci.edu/display/MASTDATA/JWST+AWS+Bulk +Download+Scripts
[4] https://github.com/gbrammer/grizli/pull/107

[5] https://github.com/mtakahiro/bbpn
[6] https://reproject.readthedocs.io/en/stable/

Table 1
5σ-limiting Magnitudes

ID	WDF-C	WDF-P
ACS F435W	27.2	⋯
ACS F606W	28.1	⋯
ACS F814W	27.5	⋯
WFC3 F105W	28.1	⋯
WFC3 F125W	27.9	⋯
WFC3 F140W	27.9	⋯
WFC3 F160W	27.8	⋯
NIRCam F090W	28.4	28.5
NIRCam F150W	28.5	28.8
NIRCam F200W	28.6	28.9
NIRCam F277W	29.0	29.3
NIRCam F356W	29.2	29.4
NIRCam F444W	28.9	29.0
NIRISS F115W	28.0	⋯
NIRISS F200W	27.9	⋯

Note. Limiting magnitudes measured in $r = 0\rlap{.}''16$ apertures. WDF-C and WDF-P represent the cluster and parallel fields, respectively.

Table 2
Magnitude-zero-point Correction Factors (Section 2.2)

Instrument	Filter	Correction Factor
ACS	F435W	1.025
ACS	F606W	1.009
ACS	F814W	1.032
WFC3	F105W	1.017
WFC3	F125W	1.000
WFC3	F140W	1.044
WFC3	F160W	0.994
NIRCam	F090W	1.016
NIRCam	F150W	1.000
NIRCam	F200W	1.029
NIRCam	F277W	1.016
NIRCam	F356W	1.016
NIRCam	F444W	1.032
NIRISS	F115W	0.985
NIRISS	F200W	0.985

Note. NIRCam F150W filter is used as the pivot point. For HST filters, the correction factors here are applied after the universal correction of 1.264 for aperture correction (Section 2).

images to the WFC3-IR F160W PSF, which has a similar FWHM as of F444W. This choice was made because of significantly different PSF shapes in JWST and HST images. While this may leave systematic offsets between the two instruments, those will be removed in the following analysis (Section 2.2).

For photometric flux extraction, we run `borgpipe`, a photometric pipeline designed for HST and JWST data reduction and photometric analyses. `borgpipe` runs `SExtractor` (ver.2.25.0; Bertin & Arnouts 1996) for image detection and flux extraction, while it includes extra steps for sophisticated error estimate of images, aperture correction, and Lyman-break dropout selection of high-z candidates, as done in similar previous studies (Trenti et al. 2012; Morishita et al. 2018b). We create infrared stacks of the F277/356/444W filters as the detection image for both fields. We set configuration parameters of `SExtractor` as follows: DETECT_MINAREA 0.0162 arcsec^2, DETECT_-THRESH 1.5, DEBLEND_NTHRESH 64, DEBLEND_MIN-CONT 64, BACK_SIZE 20, and BACK_FILTSIZE 3. Fluxes are measured in the PSF-matched images within $r = 0\rlap{.}''16$ apertures, which is comparable to the PSF size in F444W. For aperture correction, we scale fluxes by multiplying $C = f_{\rm auto,F444W}/f_{\rm aper,F444W}$, where $f_{\rm auto,F444W}$ is FLUX_AUTO of `SExtractor`, measured for individual sources. The photometric magnitude limits measured for point sources are listed in Table 1.

2.2. Zero-point Correction across Filters and Instruments

Next, we aim to calibrate flux zero points of imaging data, including offsets caused by the different PSF profiles of F444W and F160W. We first correct the relative flux offset between the two telescopes by scaling pseudo F150W fluxes, $f_{140+160}$, an auto flux interpolated from the observed HST F140W and F160W fluxes, to the one for NIRCam F150W, f_{150}. We use bright and isolated objects with signal-to-noise ratio S/N > 20 taken from the photometric catalog constructed in the previous section. For the pseudo F150W fluxes, we assume a linear slope between the two HST filters and use the value at the wavelength center of the NIRCam F150W filter. We adopt the median value of the correcting factor, $f_{150}/f_{140+160} = 1.264$. We then run `eazypy`, a python wrapper

of photometric-redshift code `EaZY` (Brammer et al. 2008), to fine-tune magnitude zero points across all filters. We run redshift fitting on those with spectroscopic redshifts (Mahler et al. 2023), both cluster member galaxies and background emission line galaxies. The derived correction factor is −1.5%–4.4% relative to F150W as the pivot (Table 2), requiring only minor correction.[7] We apply the correction to the photometric catalog. For the NIRCam images in the parallel field, where no spectroscopic measurement or HST images are available, we apply the same zero-point offsets derived for the cluster field.

3. Selection of High-redshift Galaxy Candidates

In what follows, we present our selection of galaxy candidates at $z \gtrsim 7$. To make our identification of high-z candidates as comprehensive as possible, we adopt two selection methods—conventional color-cut selection and supplemental photometric-redshift (phot-z) selection. The former provides a sample of high purity, whereas the latter covers fainter sources that fall outside the color-cut boundary.

3.1. Color-cut Selection

Our first selection consists of three steps—Lyman-break color-cut selection, photometric-redshift analysis, and visual inspection. For the filters available in this study, we explore four different redshift ranges.

3.1.1. Lyman-break Color Cut

We select candidate galaxies in the following four redshift ranges enabled by six NIRCam filters available in both fields: SF090W dropouts:

$$\mathrm{S/N}_{150} > 3.0$$

$$m_{090} - m_{150} > 1.7$$

$$m_{150} - m_{200} < 0.2$$

---

[7] The derived correction factors were 30%–40% in the NIRCam filters in our original analysis using the calibration context of `jwst_0916.pmap` and the ver.1.6.0 pipeline and consistent with those reported in Rigby et al. (2022).
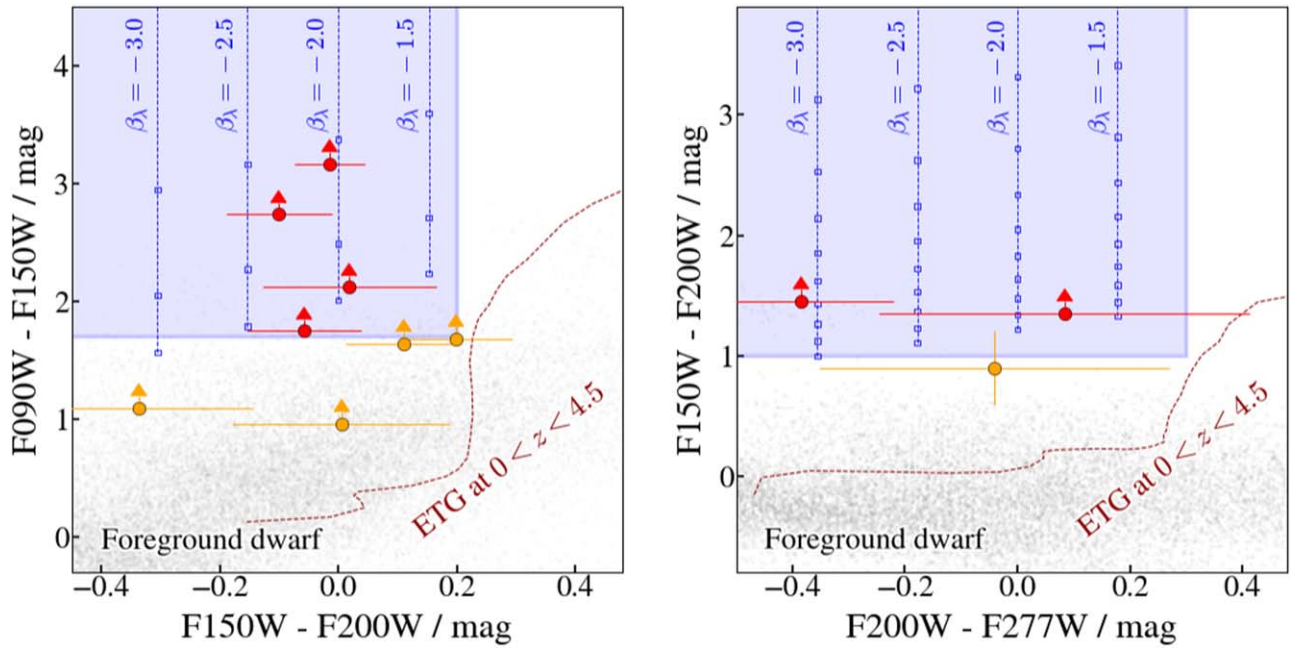
Figure 2. Final color-cut sample (red circles) and phot-z sample (orange circles), shown in two color–color diagrams for F090W-dropout sources (left) and F150W-dropout sources (right). Color tracks of sources at various redshifts are also shown—young galaxy template of different UV β_λ slopes (blue dashed lines; square symbols mark redshift, starting from $z = 7.0$ and 11.8 for the left and right panels, respectively, at an increment of $\Delta z = 0.1$), low-z early-type galaxy template (red dashed lines), and foreground dwarfs (gray dots).

$$S/N_{090\ (,\ 435,\ 606,\ 814)} < 2.0$$

F150W dropouts:

$$S/N_{200} > 3.0$$
$$m_{150} - m_{200} > 1.0$$
$$m_{200} - m_{277} < 0.3$$
$$S/N_{090\ (,\ 435,\ 606,\ 814,\ 105,\ 115,\ 125)} < 2.0$$

F200W dropouts:

$$S/N_{277} > 3.0$$
$$m_{200} - m_{277} > 1.6$$
$$m_{277} - m_{356} < 0.25$$
$$S/N_{090,\ 150\ (,\ 435,\ 606,\ 814,\ 105,\ 115,\ 125,\ 140,\ 160)} < 2.0$$

F277W dropouts:

$$S/N_{356} > 3.0$$
$$m_{277} - m_{356} > 1.4$$
$$m_{356} - m_{444} < 0.25$$
$$S/N_{090,\ 150,\ 200\ (,\ 435,\ 606,\ 814,\ 105,\ 115,\ 125,\ 140,\ 160)} < 2.0$$

In addition, we also impose $S/N > 4$ in detection images for all selections above, to minimize the fraction of artifacts. The color boundary of each selection is designed to effectively capture young, relatively dust-free galaxies at $7 \lesssim z \lesssim 11$, $11 \lesssim z \lesssim 15$, $15 \lesssim z \lesssim 20$, and $21 \lesssim z \lesssim 28$, respectively.

When NIRISS or HST images are available (i.e., in the cluster field), we supplement our selection by adding those to the nondetection filters. Potential source fluxes in the nondetection filters are also assessed in a smaller aperture, here set to $r = 0''08$ (~2.5 pixels), and the source is rejected if S/N is above the nondetection limit.

It is noted that in the F090W-dropout selection, we require nondetection in F090W (z-band dropout) while we calculate the color of Lyman break by using the flux upper limit estimated in the image in the photometric step above; thus, F090W−F150W color of the sources selected in this selection is an upper limit (Figure 2).

In Figure 2, we show color trajectories of three power-law UV slopes, $\beta_\lambda = -1.5, -2, -2.5$, and -3), where intergalactic medium (IGM) attenuation is applied by following the recipe of Dijkstra (2014). Our color-cut selection is designed to effectively minimize low-z interlopers, such as foreground dwarfs and low-z galaxy populations. Colors of dwarf stars, taken from the IRTF spectral library (Rayner et al. 2003) and the SpeX prism library (Burgasser 2014), and red galaxies (1 Gyr old, solar metallicity) at $0 < z < 4.5$ are shown.

3.1.2. Photometric-redshift Cut

We apply photometric-redshift cut to those selected in the previous color-cut section, in a similar same way as performed in previous work (Morishita et al. 2018b; Roberts-Borsani et al. 2022a; Ishikawa et al. 2022). This is to minimize the fraction of low-z interlopers such as galaxies with old stellar populations (e.g., Oesch et al. 2016) and foreground dwarfs (e.g., Morishita et al. 2020) that may migrate to the color boundary box due to photometric scatters. We run EaZY with the default magnitude prior (Figure 4 in Brammer et al. 2008), set to the filter that covers the wavelength of Lyman break. The redshift range is set to $0 < z < 30$, with a step size of $\log(1 + z) = 0.01$. By following Morishita et al. (2018b), we exclude those with $p(z < 6.5) > 0.2$, i.e., total redshift probability at $z < 6.5$ is greater than 20%.

3.1.3. Visual Inspection

Lastly, we visually inspect the sources remaining after the previous two steps. In this step, we exclude those near diffraction spikes or possible artifacts, such as flux residuals of snowballs (Rigby et al. 2022). Sources are excluded when
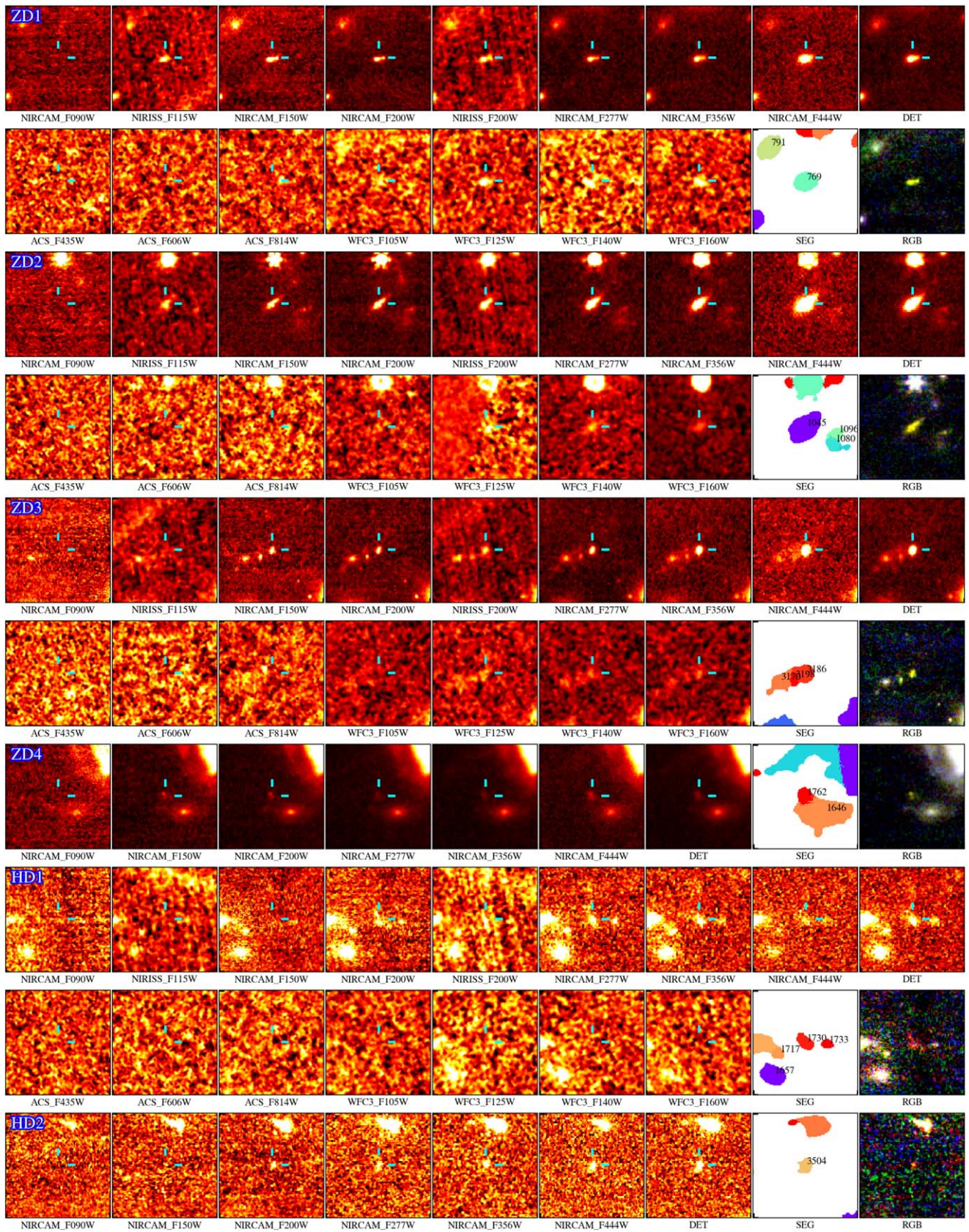
Figure 3. Postage stamps of the final color-cut sample (F090W dropouts for the first four and F150W dropouts for the following two). For each object, the top panel shows the image stamps (3.2×3.2 arcsec^2). "DET" represents the IR-stacked image. The source detection segmentation map and rgb composite (NIRCam F090W/F150W/F200W) image are also shown in the two right panels.
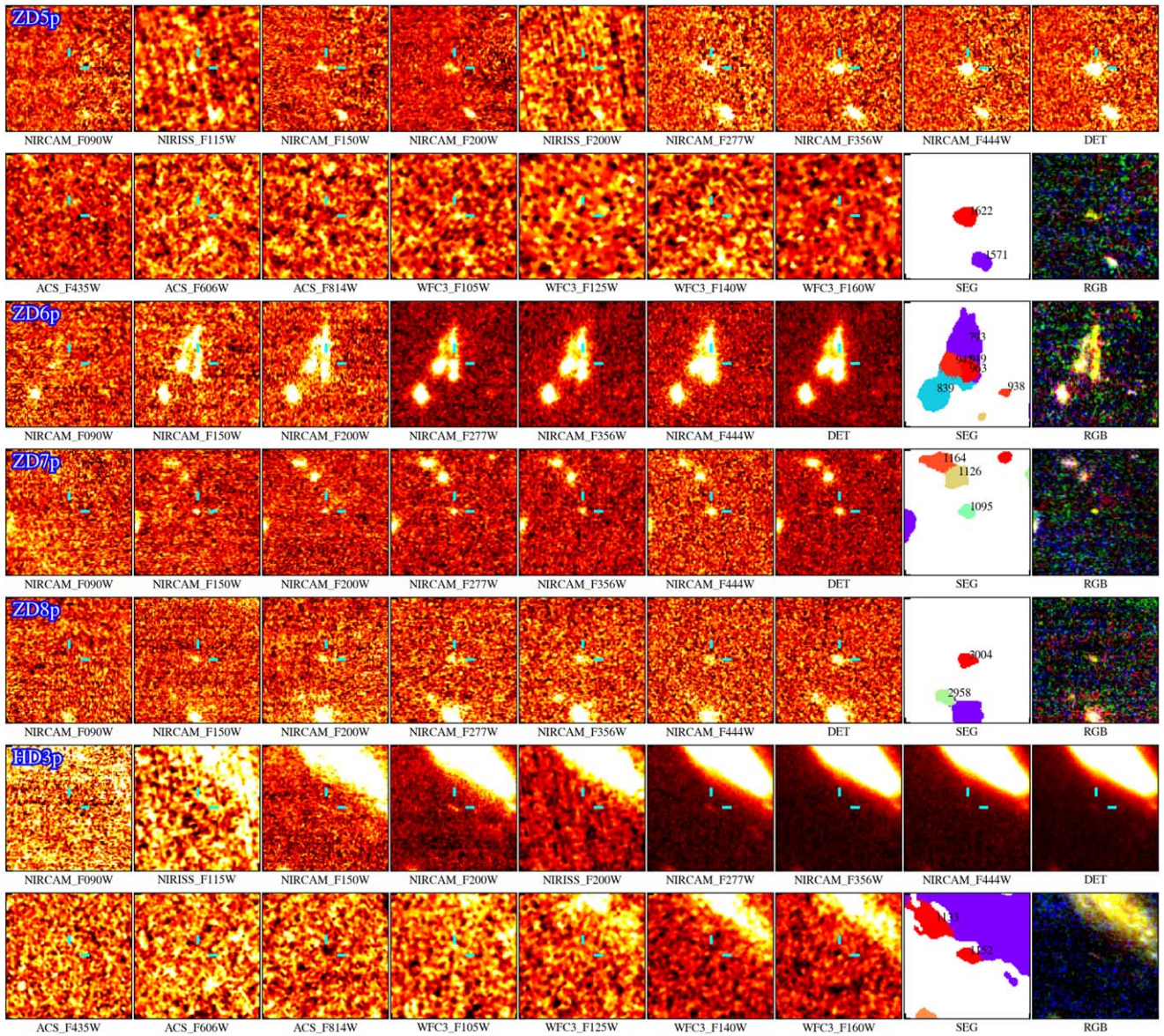
Figure 4. Same as Figure 4 but for the phot-z sample. IDs 949 and 963 are analyzed and presented as a single system, ZD6p.

either of the inspectors (T.M., M.S.) raises a flag that the object is an obvious artifact, blending with bright sources (where flux measurement would be challenging), or shows a significant amount of positive pixels in the nondetection filters. Five sources in the cluster field and 13 in the parallel fields are excluded in this step.

3.2. Supplemental Phot-z Selection

While the source selection based on the color cut is designed to provide a sample of high purity, it may not cover all possible high-z sources, especially those that are (1) near the color selection window or (2) faint, whose Lyman-break color is a relatively weak upper limit. To improve the completeness, we here aim to identify possible sources as a supplemental sample.

We run EaZY as in Section 2.2 on those detected at $S/N > 6$ in the IR-detection filter and then select those with $p(z > 6.5) > 0.8$. To further eliminate low-z interlopers, we impose nondetection ($S/N < 2$) in all filters that are blueward

to the Lyman break inferred from the derived redshift. We then visually inspect individual candidates and exclude any suspicious objects and artifacts (six and seven in the cluster and parallel fields).

4. Results

From the color-cut selection, we identified four F090W dropouts, two F150W dropouts, and none from the higher redshift bins (Figure 3). From the phot-z selection, we identify additional five sources at $7 < z < 11$ (Figure 4). Our final candidates are summarized in Table 3.

In what follows, we provide an overview of the final candidates and their physical properties obtained by spectral energy distribution (SED) and morphological analyses. For those in the cluster field, magnification factors are estimated by taking the median value of various lens models (Jullo et al. 2007; Oguri 2010; Caminha et al. 2022; Mahler et al. 2023) at the position of each source.

Table 3
List of Our Final Candidates

ID	R.A. (deg)	Decl. (deg)	$m_{\rm UV}$ (mag)	$z_{\rm phot.}$	$p(z > 6.5)$	μ [a]	Comments	Claimed[b]
				F090W dropouts ($7 \lesssim z \lesssim 11$)				
WDF-C-769/ZD1	110.8343506	−73.4345093	26.6	$7.34^{+0.05}_{-0.07}$	1.00	1.54	$z_{\rm spec.} = 7.663$	[1],[2]
WDF-C-1045/ZD2	110.8449173	−73.4350433	26.0	$8.55^{+0.15}_{-0.18}$	1.00	1.56	$z_{\rm spec.} = 7.666$	[1],[2]
WDF-C-3186/ZD3	110.8598175	−73.4491272	27.1	$9.03^{+0.31}_{-0.24}$	1.00	15.3	$z_{\rm spec.} = 8.498$	[1],[2],[3]
WDF-P-1762/ZD4	110.6461792	−73.4758453	27.9	$10.27^{+0.71}_{-0.64}$	1.00	⋯		[1],[3]
				F150W dropouts ($10 \lesssim z \lesssim 14$)				
WDF-C-1730/HD1	110.8452759	−73.4404297	28.1	$13.85^{+1.36}_{-1.39}$	0.81	2.00		[4]
WDF-P-3504/HD2	110.6964722	−73.4768295	28.5	$13.41^{+1.25}_{-1.56}$	0.98	⋯		
				Phot-z sample				
WDF-C-1622/ZD5p	110.8616486	−73.4362259	28.2	$8.21^{+1.02}_{-0.79}$	1.00	1.63		[3]
WDF-P-949/ZD6p	110.6147919	−73.4774246	27.7	$10.87^{+0.65}_{-0.64}$	1.00	⋯	Combined with WDF-P-963.	[1]
WDF-P-963/ZD6p	110.6146545	−73.4773712	28.2	$7.35^{+3.65}_{-0.18}$	0.99	⋯	Combined with WDF-P-949.	[1]
WDF-P-1095/ZD7p	110.6909027	−73.4629288	29.0	$10.58^{+0.97}_{-1.35}$	0.97	⋯		[3]
WDF-P-3004/ZD8p	110.7211685	−73.4687576	28.6	$10.02^{+1.01}_{-1.51}$	0.84	⋯		
WDF-C-1152/HD3p	110.7653885	−73.4514236	27.9	$12.70^{+2.05}_{-1.31}$	0.81	4.72	Close to a dusty galaxy at $z \sim 2.5$	

Notes. For the color-cut selection, no dropout sources other than F090W dropouts were identified. Photometric-redshift uncertainty is estimated by only using the probability distribution at $z > 6.5$. WDF-P-949 and WDF-P-963 are treated as a single system in the main text (Section 4.1.2).
[a] Median magnification of various lens models (Jullo et al. 2007; Oguri 2010; Caminha et al. 2022; Mahler et al. 2023) calculated at the position of the source.
[b] Cross-appearance of the source in other studies. 1: Adams et al. (2023) 2: Atek et al. (2023) 3: Donnan et al. (2023) 4: Yan et al. (2023). None of our samples appears in Harikane et al. (2023).

4.1. Overview of Selected Candidate Galaxies

4.1.1. The Color-cut Sample

In Figure 3, we show postage stamps of the final color-cut samples. For the five sources in the cluster field, they are not detected in the optical filters of HST in addition to their clear dropout in the F090W band. Indeed, all three of those galaxies are spectroscopically confirmed in recent work (Carnall et al. 2023; Tacchella et al. 2022), to $z = 7.663$ (ZD1), 7.665 (ZD2), and 8.498 (ZD3).

The NIRCam images resolve all candidates and reveal their morphology in detail in rest-frame UV ($\sim 0.15\ \mu m$ in F090W) to optical ($\sim 0.44\ \mu m$ in F444W). The comparison of the NIRCam images to WFC3-IR images clearly showcases the resolving power of JWST. Aside from multiband postage stamps above, in Figure 5 we also show the zoom-in image of each candidate in WFC3 F160W and NIRCam images.

ZD1 is isolated from other neighboring sources. The source consists of one primary core and a small component to its right. To provide a detailed view of this subcomponent, we perform single component Sérsic fit in the F150W image (Figure 5) using galfit (Peng et al. 2002), where we clearly see nonnegligible residuals. In the stamp of ZD2, there are two sources to the lower-right direction but they are faint and reasonably apart from ZD2, and their flux contamination to ZD2 is considered small. Same as for ZD1, single Sérsic fit reveals multiple components, including a diffuse extended component. ZD3 has two compact companions that align in one direction. SExtractor successfully deblends each of the three sources. Among the three sources, ZD3 is the brightest and thus the flux contamination is also considered small. Indeed, Sérsic fit to

ZD3, with the two close companions included simultaneously, reveals smoother residuals compared to the other two. Thus, ZD3 is characterized as compact, despite its higher magnification. We present the measured sizes in Table 4. The middle component (ID 3198 in the segmentation map) exhibits similar dropout color as for ZD3. However, we find that this object is detected in F105W, whereas ZD3 is undetected in the same band. In addition, while uncertainty is large, the photometric redshift of ID 3198 is $z \sim 1.8$. We thus conclude that, despite the proximity and the similarity in color, this object is not likely at the same redshift.

ZD4 is identified in the parallel field, with photometric redshift of $z_{\rm phot.} \sim 10.3 \pm 0.7$. While the photometric-redshift distribution extends a relatively wider range, the solution is unique to high-z, with $p(z < 6.5) \ll 1\%$. ZD4 shows extended morphology, elongated to the vertical direction. Interestingly, it shows two separate components in the F150W and F200W filters, while it is barely separated in the long channel of NIRCam, possibly due to lower spatial resolution. Since our detection is based on the F444W image, these (possible) two components are not deblended in our catalog.

In the F150W-dropout selection, we identify two candidates. HD1 shows clear nondetection in F090W, F115W, and F150W filters. The object is resolved and shows multiple components, while those components are not deblended in our detection configuration. HD2 is a faint object and flux measurements come with relatively large errors. Despite, the measured F150W-F200W color satisfies the color criterion, with the redshift probability of $p(z > 6.5) = 0.98$. It is noted that while the F150W image shows some positive pixels at the location of the object, nondetection in the band is not required in this selection.
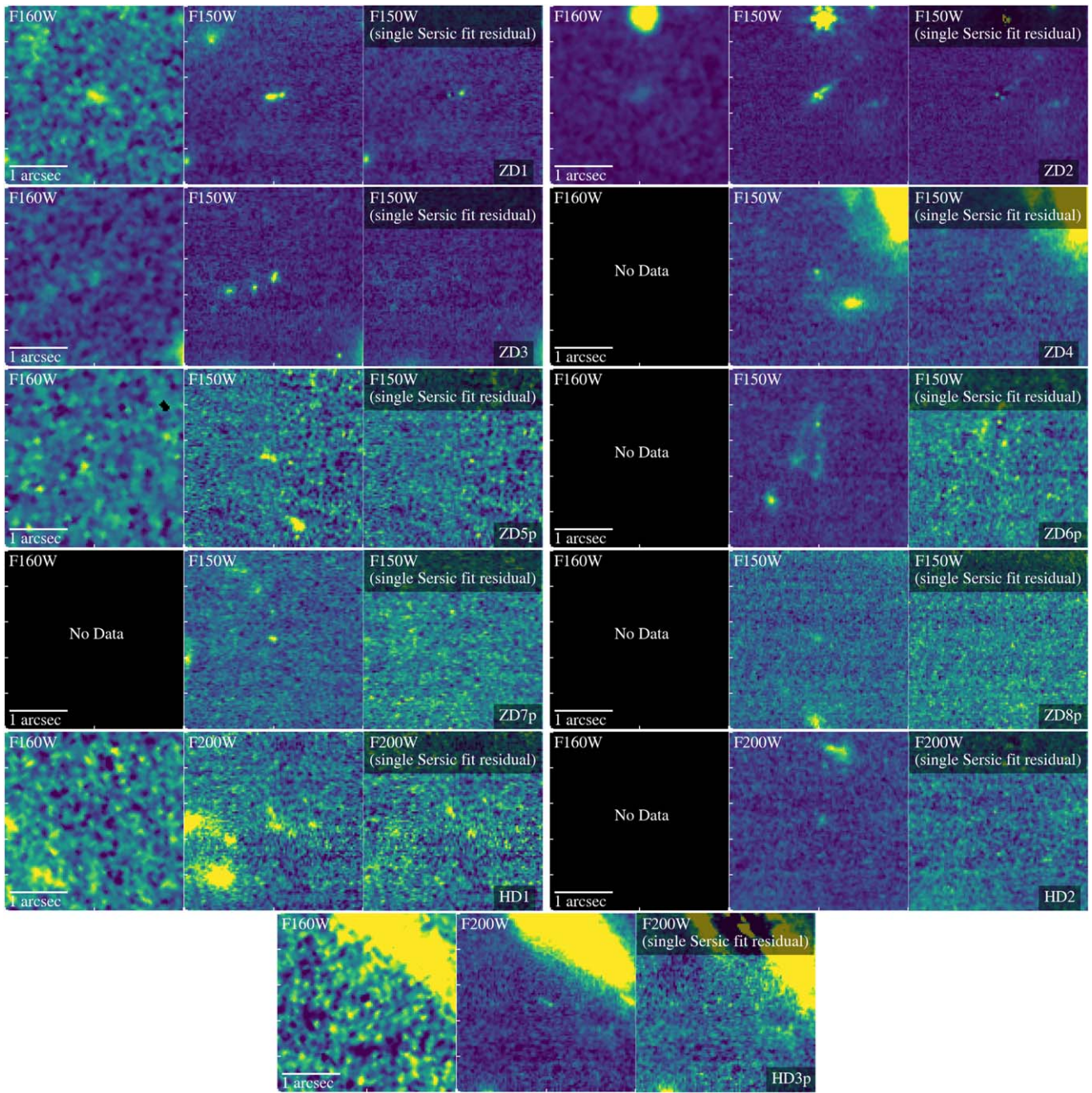
Figure 5. Zoom-in image ($3\rlap{.}{''}2 \times 3\rlap{.}{''}2$) of the final candidates at $z < 12$ (in NIRCam F150W) and $z > 12$ (NIRCam F200W). HST WFC3-IR F160W is shown for those in the cluster field. In the right panel we show the residual image after subtracting a single Sérsic component in the NIRCam image. Surrounding objects are either fitted simultaneously or masked.

Among the color-cut objects identified in the cluster field, ZD3, HD2, and HD3p were not detected in the public photometric catalog by the RELICS team.[8] ZD1 and ZD2 are detected and listed in the catalog (with their IDs 62 and 75) but with photometric redshift of $z \sim 1.6$ and 2.0. Thus, none of the four galaxies was identified as a candidate high-z source from the HST-only data set. It is worth mentioning that the two objects are flagged as detected in the ACS F606W filter in the RELICS catalog, with 2.5σ and 3.1σ, respectively, while not in the other two ACS filters (F435W and F814W). By revisiting their original F606W image, we could not confirm any

convincing detection but only a small fraction of positive pixels near the position in both cases. The false detection might have rejected those objects as a high-z candidate in their original selection.

4.1.2. The Phot-z Sample

In Figure 4, we show six galaxies (two of which are treated as a single system; see below) identified in the phot-z selection. Most of them are located near the boundary of the color selection window. Phot-z samples are in general fainter than the color-cut sample; all our phot-z samples have Lyman-break color (or upper limit) that is not red enough to be in the selection window.

---

[8] https://relics.stsci.edu

Table 4
Physical Properties of the Final Candidates

ID	z^a	M_{UV} (mag)	β_λ	$\log M_*$ ($M_\odot$)	SFR ($M_\odot$ yr^{-1})	$\log t_*$ (Gyr)	$\log Z_*$ ($Z_\odot$)	A_V (mag)	r_e (pc)	n
ZD1	7.663	$-20.05^{+0.05}_{-0.07}$	$-2.25^{+0.03}_{-0.05}$	$8.40^{+0.18}_{-0.20}$	$1.15^{+0.54}_{-0.45}$	$-1.54^{+0.53}_{-0.69}$	$-0.43^{+0.23}_{-0.43}$	$0.53^{+0.14}_{-0.18}$	119 ± 7	1.57 ± 0.37
ZD2	7.665	$-20.51^{+0.05}_{-0.05}$	$-1.77^{+0.02}_{-0.03}$	$9.03^{+0.13}_{-0.14}$	$5.74^{+1.72}_{-1.69}$	$-1.57^{+0.35}_{-0.30}$	$-0.23^{+0.07}_{-0.20}$	$0.79^{+0.23}_{-0.15}$	282 ± 8	0.37 ± 0.06
ZD3	8.499	$-17.22^{+0.08}_{-0.09}$	$-1.88^{+0.09}_{-0.07}$	$7.75^{+0.19}_{-0.15}$	$0.27^{+0.11}_{-0.07}$	$-1.94^{+0.82}_{-0.78}$	$-0.78^{+0.37}_{-0.37}$	$1.02^{+0.13}_{-0.19}$	10 ± 1	0.20 ± 0.27
ZD4	$9.78^{+1.14}_{-1.15}$	$-19.43^{+0.12}_{-0.12}$	$-1.99^{+0.28}_{-0.12}$	$8.55^{+0.59}_{-0.90}$	$0.30^{+0.66}_{-0.18}$	$-0.80^{+0.30}_{-0.70}$	$-0.48^{+0.59}_{-0.48}$	$0.20^{+0.11}_{-0.15}$	237 ± 22	0.31 ± 0.27
ZD5p	$8.65^{+0.45}_{-0.72}$	$-18.19^{+0.28}_{-0.41}$	$-1.45^{+0.42}_{-0.26}$	$8.62^{+0.51}_{-1.03}$	$1.14^{+4.21}_{-1.06}$	$-1.33^{+0.68}_{-0.58}$	$-0.81^{+0.49}_{-0.47}$	$0.67^{+0.49}_{-0.43}$	184 ± 12	0.20 ± 0.17
ZD6p	$7.58^{+0.43}_{-0.40}$	$-19.87^{+0.10}_{-0.09}$	$-1.72^{+0.06}_{-0.00}$	$8.74^{+0.09}_{-0.07}$	$3.07^{+0.62}_{-0.44}$	$-1.47^{+0.23}_{-0.27}$	$-0.09^{+0.09}_{-0.05}$	$0.49^{+0.13}_{-0.08}$	176 ± 23	1.55 ± 0.91
ZD7p	$10.50^{+1.06}_{-0.96}$	$-18.52^{+0.16}_{-0.26}$	$-1.89^{+0.19}_{-0.08}$	$8.87^{+0.32}_{-0.67}$	$0.64^{+1.87}_{-0.47}$	$-0.74^{+0.25}_{-0.95}$	$-0.90^{+0.72}_{-0.74}$	$0.58^{+0.60}_{-0.38}$	101 ± 18	0.20 ± 0.78
ZD8p	$10.01^{+0.96}_{-1.15}$	$-18.51^{+0.22}_{-0.35}$	$-1.93^{+0.32}_{-0.11}$	$8.54^{+0.34}_{-0.42}$	$1.27^{+1.39}_{-0.99}$	$-1.13^{+0.47}_{-0.67}$	$-1.17^{+0.91}_{-0.52}$	$0.67^{+0.54}_{-0.50}$	217 ± 31	0.40 ± 0.44
HD1	$13.62^{+1.27}_{-1.22}$	$-19.18^{+0.19}_{-0.21}$	$-1.99^{+0.20}_{-0.11}$	$8.51^{+0.43}_{-0.40}$	$1.25^{+1.70}_{-0.68}$	$-1.27^{+0.55}_{-0.61}$	$-1.06^{+0.91}_{-0.68}$	$0.45^{+0.34}_{-0.27}$	160 ± 29	0.55 ± 0.37
HD2	$13.16^{+1.36}_{-0.91}$	$-18.99^{+0.22}_{-0.30}$	$-1.47^{+0.04}_{-0.07}$	$8.56^{+1.04}_{-0.86}$	$0.65^{+3.48}_{-0.57}$	$-0.89^{+0.32}_{-0.66}$	$-0.43^{+0.59}_{-1.24}$	$0.41^{+0.66}_{-0.22}$	129 ± 13	0.20 ± 0.50
HD3p	$13.45^{+1.12}_{-1.40}$	$-18.23^{+0.19}_{-0.28}$	$-2.30^{+0.16}_{-0.12}$	$7.94^{+0.47}_{-0.45}$	$0.30^{+0.49}_{-0.19}$	$-1.29^{+0.59}_{-0.80}$	$-1.03^{+0.96}_{-0.68}$	$0.52^{+0.47}_{-0.37}$	29 ± 6	0.20 ± 0.76

					Median Value					
$7 < z < 14$ (all)	9.78	-18.99	-1.89	8.55	1.14	-1.29	-0.78	0.53	160	0.31
$7 < z < 10$ ($N = 6$)	8.08	-19.65	-1.82	8.59	1.15	-1.50	-0.45	0.60	180	0.34
$10 < z < 14$ ($N = 5$)	13.16	-18.52	-1.93	8.54	0.65	-1.13	-1.03	0.52	129	0.20

Note.
[a] Posterior redshift derived by gsf. ZD1, ZD2, and ZD3 are fixed to spectroscopic redshift during the fit. r_e: circularized effective radius. n: Sérsic index. t_*: mass-weighted age. Z_*: mass-weighted metallicity. Measurements are corrected for magnification.

HD3p and ZD5p are identified in the cluster field. HD3p shows an elongated morphology. The lens model indicates strong stretch at $\sim45°$ direction, which aligns with the observed elongation. It is noted that while the F150W image shows some positive pixels at the location of the object, detection is marginal (S/N$_{150} \sim 1.8$). While HD3p is located next to a bright galaxy at $z_{phot} = 2.5$ (ID 777), we consider that there is limited contribution to the measured fluxes by the foreground galaxy; ID 777 shows significant dust attenuation ($A_V \sim$ mag), which may make the SED of HD3p red. However, the best-fit model of HD3p shows blue UV slope ($\beta_{UV} \sim -2.3$), with young population of $\sim10\%$ solar metallicity with small dust attenuation ($A_V \sim 0.5$). Thus, we conclude that the flux contamination by ID 777 to HD3p remains insignificant. ZD5p is an isolated system but shows multiple components, clearly resolved in the NIRCam F200W stamp image. All components clearly drop out in F090W.

In the parallel field, three galaxies are identified. Among those, IDs 949 and 963 are of particular interest sources, being located next to each other. While SExtractor deblends those into two different objects, for their proximity and similarity in color (including clear dropout in F090W), we treat the two objects (949+963; ZD6p) as a single system in the SED fitting analysis below. It is noted that to its northern part, there is another object (ID 793) of a similar color. We did not include this segment in our photometric analysis, because of some residual flux that appears in the dropout band. We attribute this segment to the galaxy at its west (ID 942), whose redshift is $z_{phot.} \sim 5$.

The remaining two phot-z candidates, ZD7p and ZD8p, are isolated and compact. ZD8p shows a small subcomponent to its west in three filters (F200W, F277W, and F356W), but this small component is not visible in F150W. None of the phot-z candidates in the cluster field (ZD5p and HD3p) are listed in the RELICS catalog.

4.2. Spectral Energy Distribution Fitting

To investigate the physical properties of the selected candidates, we conduct spectral energy distribution fitting. We use SED fitting code gsf [9] (Morishita et al. 2018a, 2019). For those with spec-z, we set redshift as a fixed parameter during fitting. For the others, we set redshift as a free parameter within the 16th–84th percentile range derived by EaZY (Table 3). We use a template library generated by fsps (Conroy et al. 2009), with the dust attenuation law derived for the SMC (Gordon et al. 2003). We adopt a nonfunctional form for the star formation history as presented in Morishita et al. (2019) and Morishita (2021), with the age pixels set to [1, 3, 10, 30, 100, 300] Myr. This configuration allows flexibility in determining the star formation history and provides a clear insight into the stellar populations that consists of the observed SED. During our initial test, we found that the inclusion of emission lines is crucial to successfully fit the observed fluxes. We add an emission component to our fitting model, with two free parameters; ionization parameter set to $\log U \in [-3 : -1]$, and the amplitude of this component.

We show the results of SED analyses in Figure 6 and summarize the derived physical parameters in Table 4. All galaxies are in general fitted well with young stellar populations. The unprecedented coverage up to 5 μm by NIRCam reveals flux excess in the F444W filter, which is attributed to significant emission lines. For galaxies at $7 < z < 9$ (ZD1, ZD2, ZD3, ZD5p, ZD6p for our case), strong emission lines such as [O III] doublet and Hβ fall in the wavelength range of F444W and can be seen as flux excess. The observed excess in the $m_{F356W} - m_{F444W}$ color of those galaxies clearly indicates intense star formation and hot interstellar medium (e.g., Morishita et al. 2020; Roberts-Borsani et al. 2020; Leethochawalit et al. 2023) and provides
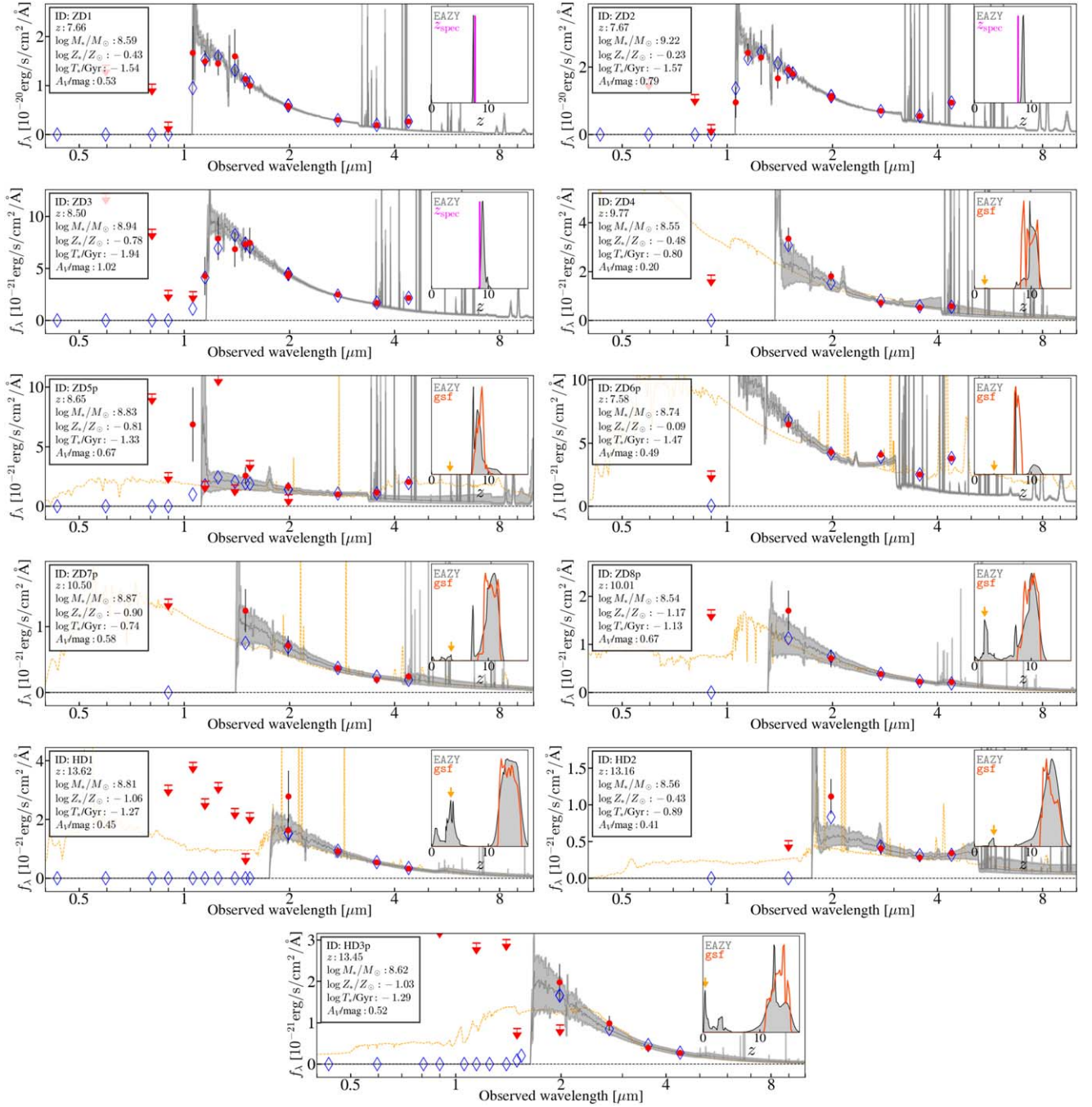
---

[9] https://github.com/mtakahiro/gsf

Figure 6. Spectral energy distribution of the final candidates. The best-fit and the 16th–84th percentile range are shown (gray line and hatched region). 2σ error is shown along with the photometric fluxes (red symbols). Blue diamonds represent the model fluxes of the corresponding filter. Photometric-redshift probability distribution (gray for EaZY and red for gsf) is shown in the inset. For those with spectroscopic redshift available (magenta vertical lines in the $p(z)$ panel), redshift is fixed during the SED fitting process. The best-fit model at the secondary peak at low redshift (indicated in the $p(z)$ panel with an arrow) is also shown in the background (orange dashed line). It is noted that fluxes and best-fit parameters are not corrected for lens magnification in the figure.

clues to metallicity (e.g., Schaerer et al. 2022; Tacchella et al. 2022). While direct inference of their emission properties is limited to the three spec-z sources, the observed blue UV slope, $\beta_{\rm UV}$, of our sample is large in negative, with the median value of ~ -1.9, which is consistent with strong line emitters found in the literature (Bouwens et al. 2014; Yamanaka & Yamada 2019; Nanayakkara et al. 2022). It is also known that $\beta_{\rm UV}$ has a negative trend both with redshift and $M_{\rm UV}$ (Bouwens et al. 2014); however, we do not observe such a

trend among our sample, likely due to the limited number of galaxies.

To further investigate the physical properties of the candidate galaxies, we derive star formation rate surface density, $\Sigma_{\rm SFR} = {\rm SFR}/2\pi r_e^2$, which is a good proxy for star formation activity within the system (e.g., Oesch et al. 2010; Ono et al. 2013). We use half-light radius derived by galfit and star formation rate calculated by averaging the last 100 Myr of the posterior star formation history. In Figure 7, we show $\Sigma_{\rm SFR}$ as a
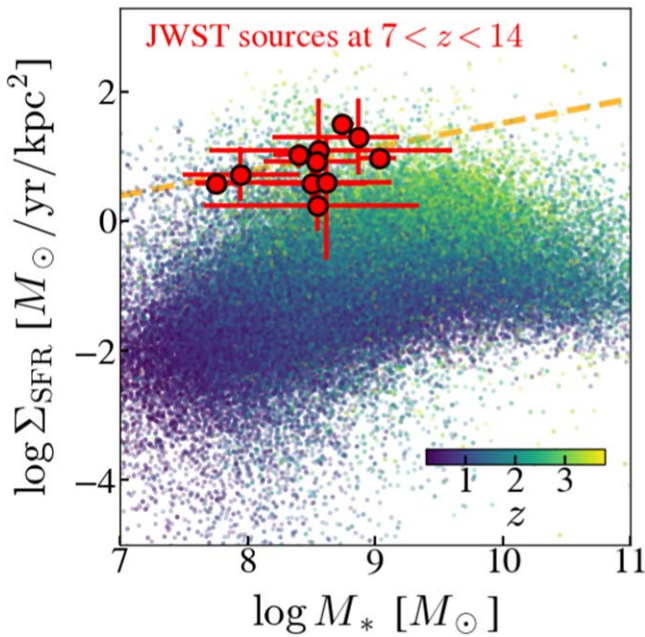
Figure 7. Star formation rate surface density of our final galaxy candidates plotted as a function of stellar mass (red circles). For comparison, galaxies at $0.2 < z < 4$ taken from the 3DHST catalog are shown. Our sample shows a moderate correlation with stellar mass. The measured linear slope ($\sim$0.38; dashed line) is shown.

function of stellar mass, along with low-z galaxies taken from the 3DHST catalog (Skelton et al. 2014; van der Wel et al. 2014; Whitaker et al. 2014). As expected from the shape of SEDs and the flux excesses in F444W, our candidates are located at the high locus of the distribution at the similar stellar mass. The observed increase in $\Sigma_{\rm SFR}$ compared to lower-z sources is likely driven both by compact morphologies (see also Yang et al. 2022) and intense star formation at high redshifts. The observed increase in star formation surface density indicates even stronger feedback in individual systems at the redshift range. Among our sample, a weak trend of $\Sigma_{\rm SFR}$ with stellar mass is seen, with the measured slope of $\sim$0.38. The Spearman's test indicates a moderate correlation, $R = 0.54$ with p-value of 0.08. A follow-up investigation with a larger sample is of particular interest, as it may hint at the efficiency of star formation in systems of different stellar (and halo) masses.

5. Discussion

In the previous sections, we present our high-z galaxy candidates identified in the first deep images of JWST. Despite the limited search volume with a single pointing, we have identified 11 photometric candidates (including three spectroscopically confirmed), two of which are $z \sim 13$, beyond the previous redshift limit enabled by Hubble (e.g., Oesch et al. 2018; Bouwens et al. 2021). Several teams report independent identification of high-z galaxy candidates in the same field (Harikane et al. 2023; Adams et al. 2023; Atek et al. 2023; Donnan et al. 2023; Yan et al. 2023). High-z source selection is extremely sensitive to detailed processes during selection and the final list may vary from one to another. Therefore, it is of particular interest to investigate if our identification of 11 sources is consistent with predictions by theoretical/empirical models and if our candidates are consistent with those identified in other studies.

5.1. Number Densities of High-redshift Candidates

In Figure 8, we show our estimates of source number density at three redshift ranges, $z \sim 9$ (F090W-dropout), $z \sim 12$ (F150W-dropout), and $z \sim 17$ (F200W-dropout). The number density is calculated as a function of absolute UV magnitude, $M_{\rm UV}$. The effective volume is calculated by running simulations, in the same way as in (Morishita et al. 2018b), for each of the color-cut selections. Briefly, we inject 100 artificial sources in random empty regions of the actual NIRCam images (and HST+NIRISS images in the cluster pointing) for every bin in redshift $\in [6:30]$ (with a logarithmic step of 0.02) and F444W magnitude $\in [26:32]$ (with a linear step of 0.2). The SED of each source is modeled by a single slope, $\beta_{\rm UV}$, with a value randomly taken from a normal distribution of $\sigma = 0.25$ centered at -2.0. The source light profile has been modeled by a single component Sérsic profile, with the size derived by the formula in Bouwens et al. (2017) for a given UV absolute magnitude.

We calculate the detection completeness as a function of apparent F444W magnitude, $C(m)$, and the source selection function as a function of magnitude and redshift, $S(z, m)$. The effective comoving volume is then calculated as

$$V_{\rm eff}(m) = \int_0^\infty S(z, m) C(m) \frac{dV}{dz} dz, \qquad (1)$$

where dV/dz represents differential comoving volume at redshift z over the effective area (where weight map is nonzero). In the cluster field, we correct the effective area and then the volume estimate for magnification. The corrected effective area is calculated on the source plane. The effective volume is corrected by redistributing the calculated volume at a given $M_{\rm UV}$ bin into the intrinsic (i.e., demagnified) magnitude bin over the effective area. For these corrections, we use the latest version of public magnification maps provided by Zitrin's team through the RELICS collaboration. To estimate a number density at each magnitude bin, we use the best-fit redshift and absolute UV magnitude derived by gsf reported in Table 4. The number densities of galaxies in the four redshift bins are reported in Table 5.

Our number density estimate at $z \sim 9$ is in good agreement with previous studies in the literature (Stefanon et al. 2017; Morishita et al. 2018b), as well as recent those in JWST fields (Harikane et al. 2023; Donnan et al. 2023). We also see agreement with the empirical prediction by Mason et al. (2015, 2023) for the Sheth et al. (2001) halo mass function. At $z \sim 9$, the model that includes dust seems to better fit the number densities estimates here and in the literature. At higher redshift, those two models are inseparable mostly due to the lack of data points at the bright end ($M_{\rm UV} < -20$).

At $z \sim 12$, where we identified three candidates, our number density estimate is slightly larger than the two JWST studies (Harikane et al. 2023; Donnan et al. 2023) and the prediction by Mason et al. (2023) but is still consistent within the uncertainty. It is noted that the two JWST studies explore not only the SMACS field but also CEERS (four pointings), GLASS (one pointing), and the Stephan's Quinted field (only in Harikane et al. 2023), resulting in $\gtrsim 5 \times$ larger volume than explored here. For the limited volume, our finding of two candidates in a single pointing may be attributed to cosmic variance. In fact, Harikane et al. (2023) identify three $z \sim 12$
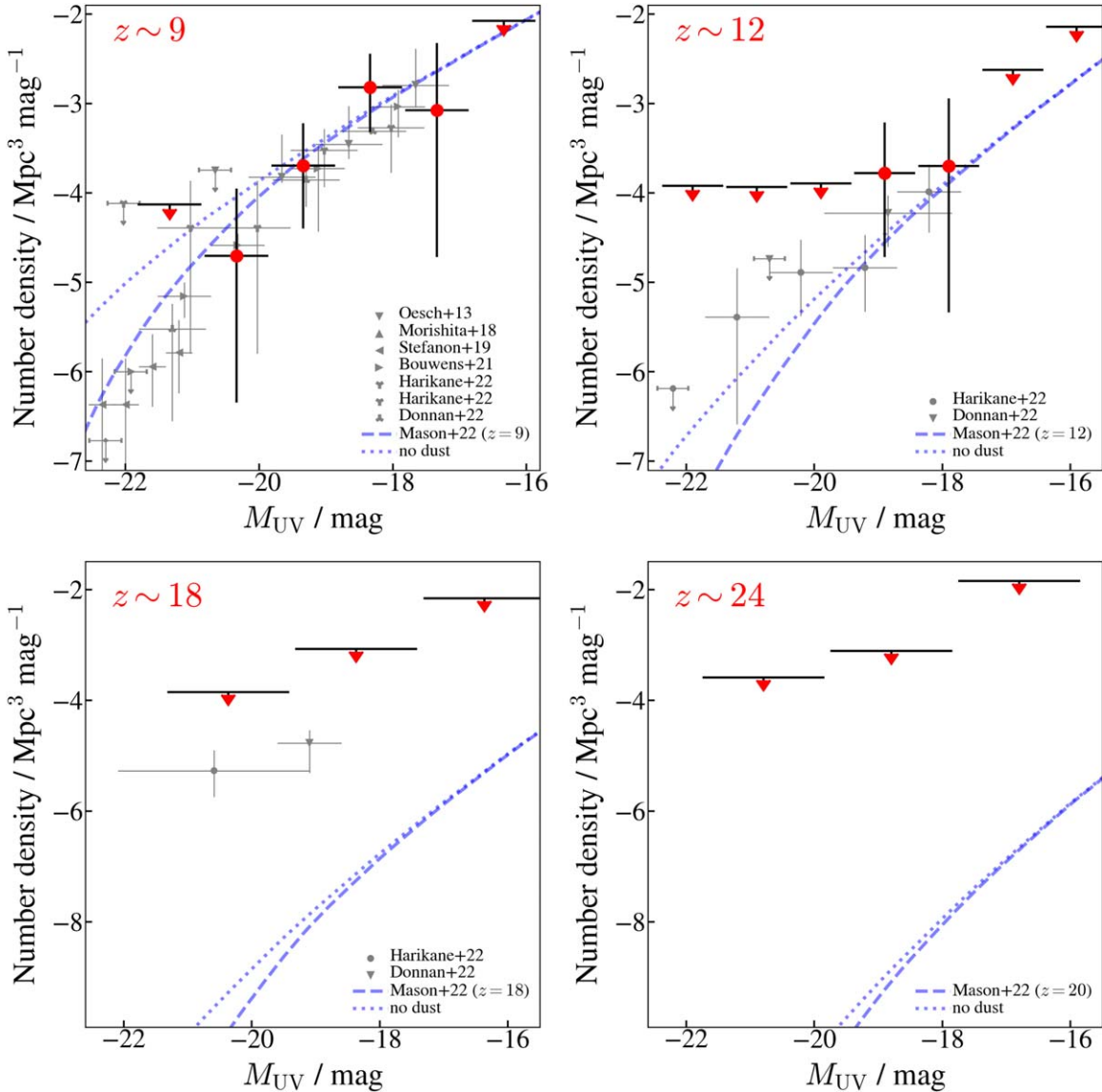
Figure 8. Number density estimates of the F090W-dropout ($z \sim 9$, top left panel) and F150W-dropout ($z \sim 12$, top right) candidates. Upper limits for the number density of F200W-dropout and F277W-dropout sources, none of which are identified here, are also shown ($z \sim 18$, bottom left and $z \sim 24$, bottom right). Error bars and upper limits represent 2σ uncertainties. Predicted luminosity functions at the corresponding redshift (Mason et al. 2015, 2023, dashed and dotted lines for the models with and without dust, respectively) shown in each panel.

candidates in one field while none in another field. The same is true in Donnan et al. (2023), where they identify two candidates at $z \sim 12$ in the SMACS field, while none in the three of the CEERS's pointings. It is also worth mentioning that that none of our $z \sim 13$ candidates are identified in either of the two studies (but one, HD1, is identified by Yan et al. (2023); see below).

At $z \sim 18$ and ~ 24, where we identified no candidate, only upper limits are shown. For the volume investigated here, it is reasonable not to identify any candidates, as the prediction goes by an order of $\gtrsim 3$ below the volume here, requiring $\sim 100 \times$ more volume to find one.

We note that the estimated number densities above are not corrected for potential contamination by low-z interlopers. Such correction would require a comprehensive setup of galaxies at low z based on the observed quantities, as well as previously underrepresented populations, which ought to be discussed in a dedicated study (e.g., Naidu et al. 2022a;

Fujimoto et al. 2022). We, however, discuss potential contributions by such low-z interlopers in the Appendix.

5.2. Comparison to Candidates from Other Studies

Here we investigate the consistency of the final list in multiple studies and what makes a difference by visiting all published candidates. All candidates from the literature studies are summarized in Table 6, along with the IDs crossmatched with our catalog. It is noted that as of the writing of this manuscript, all but one of the five studies bases their analyses on the reference files in the context of `jwst_916.pmap`. As we have found in this study, the latest set of the reference files changed flux estimates for as high as $\sim 40\%$ from the original release of the data. We thus caution the readers that their future updates with the latest reference files may change their final list of high-z candidates and may cause mismatch in our discussion here.

Table 5
Number Densities of High-z Candidates

M_{UV} (mag)	Number Density (logMpc^{-3} mag^{-1})
	$z \sim 9$
-21.34	< -4.13
-20.34	$-4.40^{+0.57}_{-0.94}$
-19.34	$-3.87^{+0.57}_{-0.94}$
-18.34	$-2.82^{+0.37}_{-0.50}$
-17.34	$-3.08^{+0.75}_{-1.64}$
-16.34	< -2.07
	$z \sim 12$
-21.90	< -3.92
-20.90	< -3.93
-19.90	< -3.89
-18.90	$-3.78^{+0.57}_{-0.94}$
-17.90	$-3.70^{+0.75}_{-1.64}$
-16.90	< -2.63
-15.90	< -2.14
	$z \sim 18$
-20.37	< -3.85
-18.37	< -3.07
-16.37	< -2.16
	$z \sim 24$
-20.80	< -3.58
-18.80	< -3.11
-16.80	< -1.84

Note. 2σ uncertainties are quoted.

5.2.1. Adams et al.

Adams et al. (2023) identify seven objects at $9 < z < 12$ via photometric-redshift selection using six NIRCam filters in the SMACS0723 field. Their selection also imposes a conservative magnitude limit ($m > 28.4$), which includes only candidates with strong Lyman-break color. All of their objects are detected in our catalog, five of which remain as the final candidates in our study. Despite the difference in photometric-redshift code used, their redshifts are broadly consistent with ours. The only exception is ID 1514 (ZD6p), whose redshift is estimated to 9.85. While our phot-z probability distribution also shows a secondary peak at $z \sim 10$, we find that the best-fit template at $z = 7.7$ consistently explains the observed flux "bumps" at $>2\,\mu$m, likely caused by a negative Balmer break between F277W and F356W and strong line emissions captured in F444W.

The other two objects are not selected in our final list of high-z candidates, primarily because of a strong low-z peak (their IDs 6115 and 10234) and suspicious positive noise in F090W (ID 10234). The SED of ID 6115 is fit well with an old galaxy template at $z \sim 2.1$. The SED of ID 10234 is fit well with a strong line emitter at $z \sim 3.1$, where we find that its flux excess in F200W is attributed to strong Hβ+[O III] emission. They limit their study to $z < 12$, and thus none of our three galaxies at $z > 12$ appear in their study.

5.2.2. Atek et al.

Atek et al. (2023) present two $z \sim 16$ candidates, two at $z \sim 12$, and seven at $9 < z < 11$, from color-cut selection, and

four additional phot-z candidates at $z \sim 11$, from the SMACS0723 field. In addition to the NIRCam filters, they combined the two NIRISS filters (F115W and F200W) to improve the redshift accuracy. Among 15 of their candidates, only three are found in our final list. The majority of their objects (10) are rejected here because of significant low-z probability. Despite clean nondetection in F090W, SMACS_z16a barely misses our phot-z selection ($p(z > 6.5) = 0.74 < 0.8$). The relatively high low-z probability is due to the faintness of the source, resulting in its flux estimate being relatively uncertain. Use of multiple phot-z estimators may recover such sources at the boundary. The other two (SMACS_z12b, SMACS_z16b) have suspicious positive noise in the nondetection filters for their redshift solutions (F090W and F150W, respectively).

5.2.3. Donnan et al.

Donnan et al. (2023) present identification of galaxies in three public fields, SMACS0723, CEERS (Finkelstein et al. 2022), and GLASS-ERS (Treu et al. 2022). From the SMACS0723 field, they identify 16 candidates at $z > 8.5$ via spectral energy distribution fitting supplemented with 2σ nondetection in blue filters. Thus, their candidate list does not include ZD1 and ZD2. Among their 16 candidates, four remain in our final list, including ZD3 with $z_{spec} = 8.5$. Nine of their candidates are excluded here due to high phot-z probabilities at $z < 6.5$. While one (their ID 38681) has relatively high probability, $p(z > 6.5) = 75\%$, its peak redshift is $z = 6.7$ with a tail extending to $z < 6.5$, making itself at lower z compared to the galaxies in our final list. Two (38697, 12682) were excluded by our visual inspection. The former object is in a crowded region of two merging galaxies, likely a part of the merging remnants. The latter object shows a suspicious noise structure in the nondetection filter F090W. Lastly, ID 6486 is a faint object ($m_{200} = 29.7$), and does not satisfy our detection limit (S/N$_{det} = 3.8 < 4$).

5.2.4. Harikane et al.

Harikane et al. (2023) perform identification of galaxies in four public fields, SMACS0723, CEERS, GLASS-ERS, and the Stephan's Quintet field. They applied two color-cut selections for $z \sim 12$ (F150W-dropout) and $z \sim 17$ (F200W-dropout) in the SMACS0723 fields, and identify one candidate at $z \sim 11.5$ and one possible candidate at $z \sim 15.6$.

SM-z12-1 is detected in our catalog and satisfies nondetection criteria in F200W and bluer bands. However, the object is faint ($m_{277} = 29.4$) and does not satisfy our detection limit (S/N$_{277} = 2.5 < 3$). The Lyman break is also not large enough to satisfy our criterion (F200W$-$F277W $= 1.2 < 1.6$). SM-z17-1 is also detected in our catalog and satisfies nondetection criteria in F200W and bluer bands. The Lyman break is not large enough to pass the limit (F200W$-$F277W $= 1.2$). We note, however, that both objects have relatively high $p(z)$ values (0.77 and 0.78, respectively) and barely miss our phot-z selection. As for SMACS_z16a in Section 5.2.2, phot-z estimates by another phot-z code may recover those two objects as final candidates.

It is worth noting that none of our two $z \sim 13$ color-cut candidates are selected in Harikane et al. (2023). While they adopt different color-cut criteria for F150W-dropout sources, we confirm that both candidates satisfy their conditions. One

Table 6
List of High-z Candidates Identified in the Literature

$ID_{liter.}$	R.A. (deg)	Decl. (deg)	$z_{liter.}$	ID	z	$p(z > 6.5)$	Comments
				Adams et al.			
1696	1.1083435e+02	−7.3434509e+01	9.59	WDF-C-769	$7.34^{+0.05}_{-0.07}$	1.00	
2462	1.1084492e+02	−7.3435043e+01	9.50	WDF-C-1045	$8.55^{+0.15}_{-0.18}$	1.00	
6878	1.1085982e+02	−7.3449127e+01	9.59	WDF-C-3186	$9.03^{+0.31}_{-0.25}$	1.00	
1514	1.1061509e+02	−7.3477554e+01	9.85	WDF-P-963	$7.35^{+3.65}_{-0.18}$	0.99	
2779	1.1064618e+02	−7.3475845e+01	9.51	WDF-P-1762	$10.26^{+0.72}_{-0.66}$	1.00	
6115	1.1071698e+02	−7.3464973e+01	10.94	WDF-P-2289	$2.05^{+8.04}_{-1.12}$	0.17	$p(z)$
10234	1.1066535e+02	−7.3501740e+01	11.42	WDF-P-6576	$3.05^{+0.27}_{-2.81}$	0.03	$p(z)$. Suspicious noise in F090W.
				Atek et al.			
SMACS_z10a	1.1085982e+02	−7.3449127e+01	9.92	WDF-C-3186	$9.03^{+0.31}_{-0.25}$	1.00	
SMACS_z10b	1.1084492e+02	−7.3435043e+01	9.79	WDF-C-1045	$8.55^{+0.15}_{-0.18}$	1.00	
SMACS_z10c	1.1083435e+02	−7.3434509e+01	9.94	WDF-C-769	$7.34^{+0.05}_{-0.07}$	1.00	
SMACS_z11c	1.1075713e+02	−7.3448654e+01	11.22	WDF-C-629	$3.02^{+7.79}_{-1.56}$	0.34	$p(z)$
SMACS_z16a	1.1086060e+02	−7.3467911e+01	15.97	WDF-C-5261	$9.84^{+1.38}_{-7.33}$	0.74	$p(z)$.
SMACS_z10d	1.1069465e+02	−7.3478012e+01	9.98	WDF-P-3632	$2.34^{+2.30}_{-1.27}$	0.07	$p(z)$
SMACS_z10e	1.1068899e+02	−7.3491814e+01	10.44	WDF-P-6786	$4.62^{+6.02}_{-2.91}$	0.32	$p(z)$
SMACS_z10f	1.1073891e+02	−7.3487900e+01	10.47	WDF-P-6546	$1.92^{+1.07}_{-1.01}$	0.02	$p(z)$
SMACS_z11a	1.1066482e+02	−7.3494514e+01	10.75	WDF-P-5279	$3.70^{+7.78}_{-1.73}$	0.34	$p(z)$
SMACS_z11b	1.1072444e+02	−7.3473129e+01	11.22	WDF-P-3753	$1.99^{+0.93}_{-0.65}$	0.01	$p(z)$
SMACS_z11d	1.1065319e+02	−7.3469231e+01	11.28	WDF-P-893	$0.72^{+1.56}_{-0.40}$	0.00	$p(z)$
SMACS_z11e	1.1070534e+02	−7.3462379e+01	11.52	WDF-P-1486	$3.51^{+7.80}_{-2.07}$	0.24	$p(z)$
SMACS_z12a	1.1069765e+02	−7.3500481e+01	12.03	WDF-P-5896	$12.68^{+1.91}_{-10.04}$	0.68	$p(z)$
SMACS_z12b	1.1071779e+02	−7.3465393e+01	12.35	WDF-P-2356	$13.83^{+1.72}_{-9.35}$	0.82	suspicious noise in F090W
SMACS_z16b	1.1066457e+02	−7.3502274e+01	15.70	WDF-P-6055	$15.95^{+0.89}_{-2.15}$	0.91	detection in F150W
				Donnan et al.			
38681	1.1086747e+02	−7.3438889e+01	8.57	WDF-C-2143	$7.31^{+0.91}_{-2.21}$	0.75	$p(z)$. $z_{peak} \sim 6.7$
39556	1.1086165e+02	−7.3436226e+01	8.86	WDF-C-1622	$8.20^{+1.03}_{-0.78}$	1.00	
28093	1.1090845e+02	−7.3455986e+01	9.16	WDF-C-4967	$2.78^{+7.26}_{-2.11}$	0.32	$p(z)$
34086	1.1085982e+02	−7.3449127e+01	9.36	WDF-C-3186	$9.03^{+0.31}_{-0.25}$	1.00	
38697	1.1086647e+02	−7.3438789e+01	9.36	WDF-C-2064	$8.50^{+1.18}_{-1.11}$	0.98	merger remnant?
35470	1.1076282e+02	−7.3446548e+01	12.03	WDF-C-512	$9.47^{+3.57}_{-7.31}$	0.64	$p(z)$
40079	1.1080821e+02	−7.3434746e+01	14.28	WDF-C-237	$5.54^{+7.50}_{-3.17}$	0.45	$p(z)$
9544	1.1066106e+02	−7.3479889e+01	9.06	WDF-P-2590	$2.06^{+0.29}_{-0.26}$	0.00	$p(z)$
12682	1.1066240e+02	−7.3475121e+01	9.47	WDF-P-2194	$9.44^{+1.56}_{-2.37}$	0.86	Suspicious noise in F090W.
22480	1.1069090e+02	−7.3462929e+01	9.47	WDF-P-1095	$10.53^{+1.00}_{-1.55}$	0.97	
12218	1.1064618e+02	−7.3475845e+01	9.68	WDF-P-1762	$10.26^{+0.72}_{-0.66}$	1.00	
15019	1.1074287e+02	−7.3472061e+01	9.68	WDF-P-4203	$7.28^{+3.42}_{-5.41}$	0.53	$p(z)$
3763	1.1070474e+02	−7.3492020e+01	9.78	WDF-P-6064	$3.51^{+8.19}_{-2.94}$	0.24	$p(z)$
6200	1.1067314e+02	−7.3486275e+01	9.78	WDF-P-4247	$8.28^{+3.05}_{-6.05}$	0.60	$p(z)$
21901	1.1069484e+02	−7.3463715e+01	12.16	WDF-P-1363	$3.16^{+1.06}_{-0.56}$	0.15	$p(z)$
6486	1.1072211e+02	−7.3485748e+01	12.56	WDF-P-6773	$14.11^{+1.89}_{-9.39}$	0.81	$S/N_{det} = 3.8$
				Harikane et al.			
SM-z12-1	1.1070145e+02	−7.3476830e+01	11.52	WDF-P-3651	$12.20^{+7.25}_{-7.58}$	0.77	$S/N_{F277W} = 2.5$, F200W−F277W = 1.2
SM-z17-1[a]	1.1087592e+02	−7.3458427e+01	15.63	WDF-C-5499	$14.73^{+4.52}_{-10.57}$	0.78	F200W−F277W = 1.2
				Yan et al.[b]			
F150DB-004	1.1081004e+02	−7.3469292e+01	14.00	WDF-C-5150	$5.61^{+0.24}_{-0.22}$	0.00	$p(z)$
F150DB-007	1.1085056e+02	−7.3466286e+01	14.60	WDF-C-5204	$10.41^{+2.20}_{-9.35}$	0.59	$p(z)$
F150DB-011	1.1086408e+02	−7.3466446e+01	11.60	WDF-C-5176	$1.52^{+3.22}_{-1.06}$	0.06	$p(z)$
F150DB-013	1.1077367e+02	−7.3464104e+01	11.40	WDF-C-2937	$2.90^{+0.39}_{-2.67}$	0.00	$p(z)$
F150DB-021	1.1080333e+02	−7.3462578e+01	11.80	WDF-C-3474	$2.84^{+5.61}_{-1.14}$	0.44	$p(z)$
F150DB-023	1.1077446e+02	−7.3462074e+01	7.20	WDF-C-2724	$6.07^{+3.95}_{-4.23}$	0.46	$p(z)$
F150DB-026	1.1084926e+02	−7.3461319e+01	11.40	WDF-C-4828	$2.91^{+0.45}_{-2.57}$	0.00	$p(z)$

Table 6
(Continued)

ID$_{\text{liter.}}$	R.A. (deg)	Decl. (deg)	$z_{\text{liter.}}$	ID	z	$p(z > 6.5)$	Comments
F150DB-031	1.1083992e+02	−7.3460083e+01	11.60	WDF-C-4061	$3.90^{+7.10}_{-2.46}$	0.25	$p(z)$
F150DB-033	1.1087781e+02	−7.3459175e+01	14.80	WDF-C-5690	$3.36^{+10.80}_{-1.89}$	0.23	$p(z)$
F150DB-040	1.1080025e+02	−7.3456947e+01	10.80	WDF-C-2728	$2.80^{+0.39}_{-2.59}$	0.01	$p(z)$
F150DB-041	1.1077812e+02	−7.3457100e+01	16.00	WDF-C-2145	$0.53^{+3.42}_{-0.15}$	0.03	$p(z)$
F150DB-044	1.1091432e+02	−7.3456139e+01	11.60	WDF-C-5213	$2.61^{+0.67}_{-2.36}$	0.01	$p(z)$
F150DB-048	1.1075723e+02	−7.3455078e+01	15.00	WDF-C-1268	$6.12^{+6.47}_{-3.90}$	0.46	$p(z)$
F150DB-050	1.1085293e+02	−7.3454163e+01	11.60	WDF-C-3629	$2.93^{+0.80}_{-2.66}$	0.01	$p(z)$
F150DB-052	1.1086780e+02	−7.3453796e+01	15.00	WDF-C-3964	$12.42^{+2.01}_{-9.49}$	0.73	$p(z)$
F150DB-054	1.1080293e+02	−7.3452637e+01	11.40	WDF-C-2235	$0.48^{+0.08}_{-0.19}$	0.00	$p(z)$
F150DB-056	1.1078082e+02	−7.3452866e+01	7.20	WDF-C-1658	$11.53^{+3.21}_{-8.51}$	0.72	$p(z)$
F150DB-058	1.1085042e+02	−7.3452530e+01	15.20	WDF-C-3407	$0.27^{+0.12}_{-0.14}$	0.00	$p(z)$
F150DB-069	1.1076826e+02	−7.3448433e+01	11.80	WDF-C-865	$12.48^{+1.90}_{-9.39}$	0.77	$p(z)$
F150DB-075	1.1075976e+02	−7.3444901e+01	11.40	WDF-C-284	$2.89^{+0.31}_{-2.59}$	0.00	$p(z)$
F150DB-076	1.1087300e+02	−7.3444359e+01	11.60	WDF-C-2959	$0.93^{+2.77}_{-0.47}$	0.00	$p(z)$
F150DB-079	1.1080526e+02	−7.3441589e+01	13.80	WDF-C-931	$3.36^{+9.25}_{-0.79}$	0.38	$p(z)$
F150DB-082	1.1084528e+02	−7.3440430e+01	11.60	WDF-C-1730	$13.39^{+1.65}_{-9.37}$	0.81	
F150DB-084	1.1078188e+02	−7.3439972e+01	11.60	WDF-C-226	$4.00^{+0.92}_{-3.33}$	0.10	$p(z)$
F150DB-088	1.1080888e+02	−7.3438148e+01	11.60	WDF-C-626	$3.58^{+8.92}_{-1.28}$	0.34	$p(z)$
F150DB-090	1.1085972e+02	−7.3437157e+01	11.40	WDF-C-1643	$2.95^{+0.68}_{-1.16}$	0.00	$p(z)$
F150DB-095	1.1085355e+02	−7.3433678e+01	11.60	WDF-C-1144	$2.77^{+1.86}_{-2.01}$	0.07	$p(z)$
F150DB-C4	1.1085859e+02	−7.3444389e+01	10.40	WDF-C-2420	$15.69^{+1.10}_{-10.25}$	0.83	Likely a dusty interloper at $z \sim 4.5$.
F200DB-015	1.1078262e+02	−7.3467125e+01	16.00	WDF-C-3520	$9.68^{+10.66}_{-6.40}$	0.62	$p(z)$
F200DB-045	1.1084516e+02	−7.3461304e+01	20.40	WDF-C-4322	$0.40^{+0.15}_{-0.26}$	0.00	$p(z)$
F200DB-086	1.1077728e+02	−7.3455536e+01	15.40	WDF-C-1932	$14.60^{+5.76}_{-9.97}$	0.76	$p(z)$
F200DB-109	1.1090538e+02	−7.3453957e+01	15.80	WDF-C-5512	$0.05^{+0.04}_{-0.03}$	0.00	$p(z)$
F200DB-159	1.1085593e+02	−7.3445839e+01	16.00	WDF-C-2731	$1.97^{+0.32}_{-1.59}$	0.01	$p(z)$
F200DB-175	1.1079664e+02	−7.3443909e+01	16.20	WDF-C-999	$5.07^{+4.32}_{-3.46}$	0.34	$p(z)$
F200DB-181	1.1080309e+02	−7.3442154e+01	15.80	WDF-C-946	$4.21^{+1.03}_{-2.69}$	0.13	$p(z)$
F277DB-001	1.1082343e+02	−7.3473969e+01	−99.00	WDF-C-5008	$7.66^{+5.95}_{-5.05}$	0.55	$p(z)$

Yan et al.

ID$_{\text{liter.}}$	R.A. (deg)	Decl. (deg)	$z_{\text{liter.}}$	ID	z	$p(z > 6.5)$	Comments
F150DB-013	1.1073157e+02	−7.3465691e+01	11.40	WDF-P-2859	$1.64^{+1.64}_{-1.41}$	0.01	$p(z)$
F150DA-008	1.1067804e+02	−7.3498581e+01	13.40	WDF-P-6060	$4.07^{+3.78}_{-2.67}$	0.20	$p(z)$
F150DA-015	1.1064458e+02	−7.3491646e+01	11.80	WDF-P-4197	$7.17^{+4.08}_{-5.18}$	0.53	$p(z)$
F150DA-018	1.1069163e+02	−7.3490501e+01	6.40	WDF-P-4934	$1.81^{+0.43}_{-0.41}$	0.00	$p(z)$
F150DA-019	1.1062254e+02	−7.3489227e+01	11.60	WDF-P-2702	$1.27^{+0.20}_{-0.18}$	0.00	$p(z)$
F150DA-020	1.1069055e+02	−7.3488899e+01	11.20	WDF-P-5172	$4.15^{+0.47}_{-3.54}$	0.00	$p(z)$
F150DA-026	1.1064958e+02	−7.3486969e+01	11.00	WDF-P-3551	$0.41^{+0.20}_{-0.16}$	0.00	$p(z)$
F150DA-027	1.1071288e+02	−7.3486656e+01	7.40	WDF-P-5532	$0.67^{+0.25}_{-0.37}$	0.00	$p(z)$
F150DA-031	1.1062753e+02	−7.3484474e+01	11.40	WDF-P-2555	$3.36^{+8.78}_{-0.96}$	0.41	$p(z)$
F150DA-036	1.1071104e+02	−7.3481148e+01	11.00	WDF-P-4620	$2.88^{+1.35}_{-2.32}$	0.03	$p(z)$
F150DA-038	1.1072043e+02	−7.3480797e+01	13.40	WDF-P-4785	$0.71^{+0.52}_{-0.27}$	0.00	$p(z)$
F150DA-039	1.1071104e+02	−7.3481148e+01	7.40	WDF-P-4620	$2.88^{+1.35}_{-2.32}$	0.03	$p(z)$
F150DA-047	1.1066683e+02	−7.3481430e+01	7.40	WDF-P-3289	$8.00^{+7.32}_{-5.54}$	0.56	$p(z)$
F150DA-050	1.1064584e+02	−7.3478386e+01	13.40	WDF-P-2190	$4.60^{+5.22}_{-3.51}$	0.34	$p(z)$
F150DA-054	1.1062034e+02	−7.3476067e+01	11.40	WDF-P-930	$7.93^{+8.37}_{-5.55}$	0.57	$p(z)$
F150DA-057	1.1070329e+02	−7.3475700e+01	11.40	WDF-P-3537	$3.84^{+0.71}_{-3.24}$	0.02	$p(z)$
F150DA-058	1.1065908e+02	−7.3475243e+01	13.40	WDF-P-2102	$2.98^{+0.71}_{-2.61}$	0.00	$p(z)$
F150DA-060	1.1062808e+02	−7.3473839e+01	11.40	WDF-P-822	$6.97^{+4.58}_{-5.09}$	0.53	$p(z)$
F150DA-062	1.1068426e+02	−7.3474068e+01	11.40	WDF-P-2694	$1.47^{+0.75}_{-0.55}$	0.00	$p(z)$
F150DA-063	1.1068298e+02	−7.3474297e+01	7.40	WDF-P-2691	$3.51^{+6.45}_{-2.21}$	0.20	$p(z)$
F150DA-066	1.1062359e+02	−7.3470810e+01	11.40	WDF-P-178	$13.82^{+9.88}_{-9.12}$	0.77	$p(z)$
F150DA-077	1.1067607e+02	−7.3466461e+01	13.40	WDF-P-1210	$15.00^{+10.19}_{-10.20}$	0.78	$p(z)$
F150DA-078	1.1066418e+02	−7.3464508e+01	11.80	WDF-P-430	$2.79^{+2.46}_{-1.51}$	0.00	$p(z)$
F150DA-081	1.1066294e+02	−7.3463394e+01	13.40	WDF-P-237	$1.67^{+0.52}_{-1.60}$	0.00	$p(z)$
F150DA-082	1.1067789e+02	−7.3463089e+01	7.60	WDF-P-658	$8.38^{+9.25}_{-6.63}$	0.58	$p(z)$
F200DA-033	1.1064064e+02	−7.3488998e+01	6.40	WDF-P-3653	$7.33^{+6.28}_{-5.24}$	0.57	$p(z)$

Table 6
(Continued)

$ID_{liter.}$	R.A. (deg)	Decl. (deg)	$z_{liter.}$	ID	z	$p(z > 6.5)$	Comments
F200DA-034	1.1073029e+02	−7.3488083e+01	19.80	WDF-P-6862	$16.58^{+7.92}_{-11.24}$	0.80	$S/N_{det} = 2.5$
F200DA-040	1.1072467e+02	−7.3485855e+01	20.00	WDF-P-6327	$7.47^{+6.90}_{-5.45}$	0.54	$p(z)$
F200DA-056	1.1061219e+02	−7.3479179e+01	15.60	WDF-P-1195	$2.91^{+6.64}_{-1.90}$	0.19	$p(z)$
F277DA-001	1.1065731e+02	−7.3502014e+01	−99.00	WDF-P-7484	$0.32^{+0.16}_{-0.18}$	0.00	$p(z)$
F277DA-033	1.1070955e+02	−7.3476181e+01	−99.00	WDF-P-3715	$1.55^{+0.80}_{-0.34}$	0.00	$p(z)$
F277DA-040	1.1060577e+02	−7.3473579e+01	−99.00	WDF-P-50	$0.66^{+0.26}_{-0.25}$	0.00	$p(z)$
F277DA-044	1.1069387e+02	−7.3470459e+01	−99.00	WDF-P-2421	$0.09^{+0.22}_{-0.06}$	0.00	$p(z)$
F277DA-045	1.1067736e+02	−7.3469704e+01	−99.00	WDF-P-1729	$3.81^{+1.34}_{-1.01}$	0.01	$p(z)$

Notes.
[a] Listed as a potential candidate in their study.
[b] 80 objects that are detected in our catalog, out of 88 in the original study by Yan et al. (2023), are shown.

possible remaining factor is their additional constraint by $\Delta\chi^2 = \chi^2_{low-z} - \chi^2_{high-z} > 4$ from their SED analyses.

5.2.5. Yan et al.

Yan et al. (2023) present 88 objects as galaxy candidates at $11 < z < 20$ in the SMACS0723 field. They select their candidates via color-cut using six NIRCam filters, starting F150W as a dropout band; thus their selection does not overlap with our F090W-dropout selection. Out of their 88 sources, eight objects are found not to be listed in our parent catalog.

The majority ($N = 77$) of the remaining sources are not selected in this study due to high phot-z probabilities at $z < 6.5$. One of the objects (ID F150DB-082) remains in our list of the phot-z sample. One of the other two objects with $p(z > 6.5) > 0.8$, ID F150DB-C4, shows a significantly red SED. Our SED analysis, with redshift fixed to $z = 10.4$, Yan et al.'s (2023) value, indicates a significant dust attenuation, $A_V \sim 4$ mag, which is unlikely at this redshift. We thus conclude that, despite being $p(z > 6.5) = 0.83$, this object is a low-z interloper, likely at $z \sim 4.5$, where we observe a narrow redshift peak. The other object, F200DA-034 at $z \sim 19.8$, is very faint ($m_{356} = 29.3$) and does not pass the detection cut (S/N$_{det}$ = 2.5 < 4).

6. Summary

Already on the basis of this first data set it is clear that detections with WFC3-IR with few bands shorter than 1.6 μm are not a robust way to identify high-z galaxies as at least the two sources in the cluster field had been assigned much lower redshifts. These data also allow us to begin testing the reliability of phot-z at previously untested redshifts. More will be needed but it is comforting that three candidates identified in the cluster field on the basis of photometry alone were spectroscopically confirmed. This gives us hope that photometric selection is not seriously plagued by false detection. We cannot say at this time anything about its completeness given that the NIRSpec micro-shutter assembly slits were placed on photometrically selected objects.

We repeated the selection analyses for the cluster field with the NIRCam imaging data only. This provided the same set of color dropout galaxies selected in the first step of Section 3.1. This implies that our selection of candidates in the parallel field, despite the absence of HST coverage, is more or less of similar

quality. This is also encouraging for future searches of high-z sources with JWST alone (e.g., pure-parallel imaging programs).

The comparison with other studies over the same fields provides a cautionary tale on how to interpret results derived only through photometry: different studies with different but equally reasonable criteria can yield significant differences in the selected samples.

A final note is that our analysis may still not be complete in terms of source detection. The (in)famous hexagonal PSF spikes from bright stars severely contaminate surrounding pixels and make it challenging to detect all background sources. In addition, the cluster field is even more challenging, being affected by brightest cluster galaxies. A dedicated analysis, such as one presented in Bouwens et al. (2021), will be required for detection completeness in crowded fields.

SMACS0723 is not only the deepest NIR imaging field at this time, but also has rich spectroscopic data obtained by NIRSPEC and NIRISS as well as mid-IR imaging by MIRI collected during the ERO campaign. Future follow-up studies with those data will further reveal the nature of the three galaxies in the cluster field. While the additional candidates newly identified in this study are not as exceptionally bright as those in the cluster field, they are still within the reach of sensitive NIRSPEC spectroscopy for its strong emission lines revealed in our study.

Appendix
Number Estimate of Low-z Interlopers

The fraction of low-z contaminants among the selected sources is of particular interest. We investigate this by using JWST extragalactic mock catalogs published by the JAGUAR collaboration (Williams et al. 2018). We start with three of their realizations, each of which covers $11' \times 11'$, by fluctuating flux measurements of each filter assuming the same noise level, separately for the cluster and parallel fields. As sources in the catalogs are large enough to be resolved by JWST, we rescaled the noise level by using JWST Exposure Time Calculator, assuming various size of galaxies with a single Sérsic profile. The reprocessed catalog is then provided to our photometric pipeline to go through all steps for high-z source selection, including dropout selection and photometric-redshift analysis. We define those pass the selection but are intrinsically at $z < 6$ as contaminants.

Figure 9 shows the results. For the cluster field, the number of contaminants are low over the redshift. The primary contributors are low-mass ($\log M_*/M_\odot \sim 7$–8), faint galaxies at $z \sim 2$. By scaling the total area to the field area of the cluster

field ($2'.2 \times 2'.2$), we find that only 0.5 at $z < 11$ and <0.2 at $12 < z < 15$. There are no contaminants identified beyond the redshift, likely due to the fact that >2 NIRCam filters serve as nondetection filters.

For the parallel field, where only six NIRCam filters are available, the number of contaminants increases by a factor of ~ 2, but with a similar redshift trend as for the cluster field. The increase is likely due to the lack of nondetection filters from HST and NIRISS at the redshift range of $z < 15$; in fact, beyond the redshift, the number of contaminants decreases, likely for the same reason as for the cluster field. The total number of contaminant still remains relatively low, ~ 1.5 at $z < 12$ and ~ 0.8 at $12 < z < 15$, compared to the number of candidates identified in the main text.

While adopting more stringent criteria ($S/N_{det} > 8$ and $S/N_{UV} > 5$, instead of >6 and >3 adopted in the main text) would suppress the number of contaminants (dashed lines in the same figure), the trend stays similar for both fields. The results here indicate that the contamination is not negligible, even with our stringent, three-step selection, and that follow-up spectroscopic confirmation of published candidates in several studies is required for further conclusions on, e.g., the possible excess in the luminosity function at $z \gtrsim 12$ reported and discussed in various studies. As has been demonstrated by several more recent spectroscopic studies (e.g., Roberts-Borsani et al. 2022b; Curtis-Lake et al. 2022; Morishita et al. 2022; Wang et al. 2022; Williams et al. 2022; Fujimoto et al. 2023), JWST offers excellent ability to spectroscopically confirm high-z photometric candidates via strong optical emission lines and/or the Lyman break, within a reasonably small amount of time ($\lesssim 20$ hr).
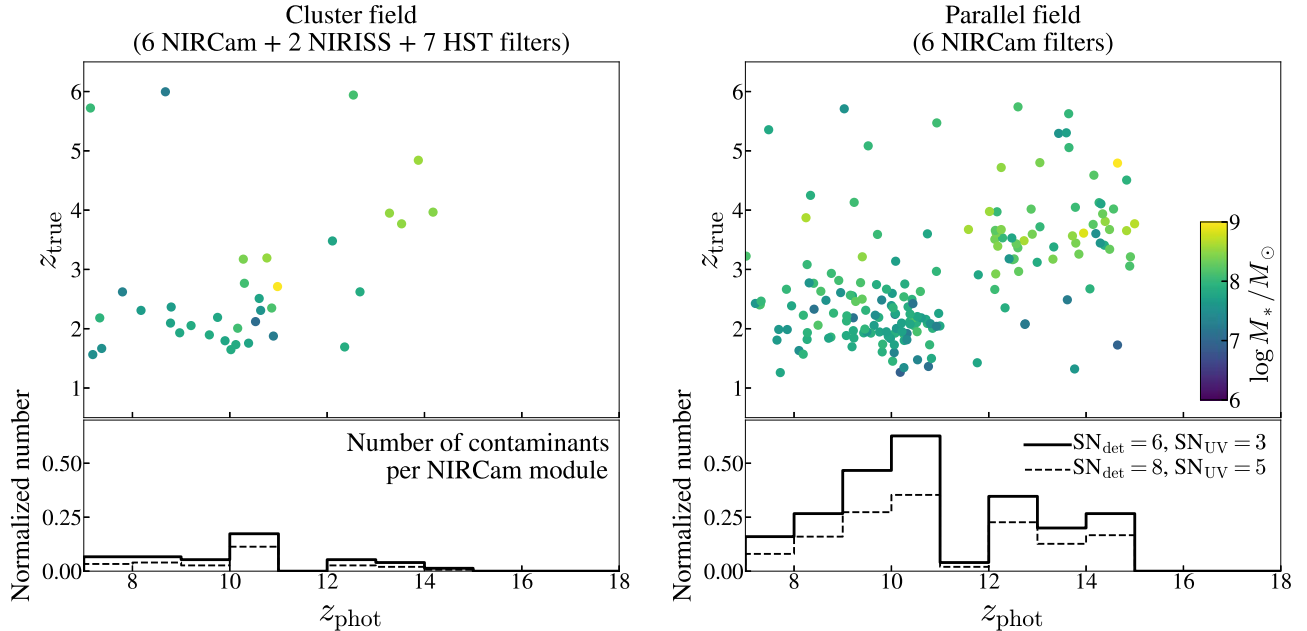

Figure 9. Distribution of low-z contaminants that are selected by our photometric dropout and phot-z ($p(z > 6.5) > 0.8$) selection. Source fluxes are simulated by adding noise to the JAGUAR extragalactic catalogs of three realizations, each of which contains $\sim 3 \times 10^5$ sources over $11' \times 11'$ area. Noted that scatter points are taken from all simulated fields (~ 363 arcmin^2 in total; see 4.8 arcmin^2 for each NIRCam module). The estimated number of low-z contaminants per redshift bin per the area of each NIRCam module is shown in the bottom panel. For the cluster field (left), the primary contributors are low-mass ($\log M_*/M_\odot \sim 7$–8) galaxies at $z \sim 2$. For the parallel field (right), where only six NIRCam filters are available, the number of contaminants increases. Having more stringent criteria (dashed lines) would help but not completely eliminate such contaminants.

ORCID iDs

T. Morishita https://orcid.org/0000-0002-8512-1404
M. Stiavelli https://orcid.org/0000-0001-9935-6047

References

Adams, N. J., Conselice, C. J., Ferreira, L., et al. 2023, MNRAS, 518, 4755
Atek, H., Shuntov, M., Furtak, L. J., et al. 2023, MNRAS, 519, 1201
Bertin, E., & Arnouts, S. 1996, A&AS, 117, 393
Boucaud, A., Bocchio, M., Abergel, A., et al. 2016, A&A, 596, A63
Bouwens, R. J., Illingworth, G. D., Oesch, P. A., et al. 2014, ApJ, 793, 115
Bouwens, R. J., Illingworth, G. D., Oesch, P. A., et al. 2015, ApJ, 803, 34
Bouwens, R. J., Illingworth, G. D., Oesch, P. A., et al. 2017, arXiv:1711.02090
Bouwens, R. J., Illingworth, G. D., van Dokkum, P. G., et al. 2021, AJ,
    162, 255
Bowler, R. A. A., Jarvis, M. J., Dunlop, J. S., et al. 2020, MNRAS, 493, 2059
Boyer, M. L., Anderson, J., Gennaro, M., et al. 2022, RNAAS, 6, 191
Bradley, L. D., Trenti, M., Oesch, P. A., et al. 2012, ApJ, 760, 108
Brammer, G. 2022, Preliminary updates to the NIRCam photometric
    calibration, Zenodo, doi:10.5281/zenodo.7143382
Brammer, G. B., van Dokkum, P. G., & Coppi, P. 2008, ApJ, 686, 1503
Burgasser, A. J. 2014, in Int. Workshop on Stellar Spectral Libraries ASI Conf.
    Ser. 11, ed. H. P. Singh, P. Prugniel, & I. Vauglin, 7
Caminha, G. B., Suyu, S. H., Mercurio, A., et al. 2022, A&A, 666, L9
Carnall, A. C., Begley, R., McLeod, D. J., et al. 2023, MNRAS, 518, L45
Castellano, M., Fontana, A., Treu, T., et al. 2022, ApJL, 938, L15
Chabrier, G. 2003, PASP, 115, 763
Coe, D., Salmon, B., Bradac, M., et al. 2019, ApJ, 884, 85
Conroy, C., Gunn, J. E., & White, M. 2009, ApJ, 699, 486
Curtis-Lake, E., Carniani, S., Cameron, A., et al. 2022, arXiv:2212.04568
Dijkstra, M. 2014, PASA, 31, e040
Donnan, C. T., McLeod, D. J., Dunlop, J. S., et al. 2023, MNRAS, 518, 6011
Finkelstein, S. L., Bagley, M. B., Arrabal Haro, P., et al. 2022, ApJL, 940, L55
Finkelstein, S. L., Papovich, C., Dickinson, M., et al. 2013, Natur, 502, 524
Fujimoto, S., Arrabal Haro, P., Dickinson, M., et al. 2023, arXiv:2301.09482
Fujimoto, S., Brammer, G. B., Watson, D., et al. 2022, Natur, 604, 261
Fukugita, M., Ichikawa, T., Gunn, J. E., et al. 1996, AJ, 111, 1748
Gordon, K. D., Clayton, G. C., Misselt, K. A., Landolt, A. U., & Wolff, M. J.
    2003, ApJ, 594, 279
Gunn, J. E., & Peterson, B. A. 1965, ApJ, 142, 1633
Harikane, Y., Inoue, A. K., Mawatari, K., et al. 2022, ApJ, 929, 1
Harikane, Y., Ouchi, M., Oguri, M., et al. 2023, ApJS, 265, 5
Hashimoto, T., Laporte, N., Mawatari, K., et al. 2018, Natur, 557, 392
Ishikawa, Y., Morishita, T., Stiavelli, M., et al. 2022, ApJ, 936, 167
Jiang, L., Kashikawa, N., Wang, S., et al. 2021, NatAs, 5, 256
Jullo, E., Kneib, J.-P., Limousin, M., et al. 2007, NJPh, 9, 447
Leethochawalit, N., Trenti, M., Santini, P., et al. 2023, ApJL, 942, L26
Madau, P., Haardt, F., & Rees, M. J. 1999, ApJ, 514, 648
Mahler, G., Jauzac, M., Richard, J., et al. 2023, ApJ, 945, 49
Mason, C. A., Trenti, M., & Treu, T. 2015, ApJ, 813, 21
Mason, C. A., Trenti, M., & Treu, T. 2023, MNRAS, 521, 497
McLeod, D. J., McLure, R. J., Dunlop, J. S., et al. 2015, MNRAS, 450, 3032

Morishita, T. 2021, ApJS, 253, 4
Morishita, T., Abramson, L. E., Treu, T., et al. 2018a, ApJL, 856, L4
Morishita, T., Abramson, L. E., Treu, T., et al. 2019, ApJ, 877, 141
Morishita, T., Roberts-Borsani, G., Treu, T., et al. 2022, arXiv:2211.09097
Morishita, T., Stiavelli, M., Trenti, M., et al. 2020, ApJ, 904, 50
Morishita, T., Trenti, M., Stiavelli, M., et al. 2018b, ApJ, 867, 150
Naidu, R. P., Oesch, P. A., Setton, D. J., et al. 2022a, arXiv:2208.02794
Naidu, R. P., Oesch, P. A., van Dokkum, P., et al. 2022b, ApJL, 940, L14
Nanayakkara, T., Glazebrook, K., Jacobs, C., et al. 2022, arXiv:2207.13860
Oesch, P. A., Bouwens, R. J., Carollo, C. M., et al. 2010, ApJL, 709, L21
Oesch, P. A., Bouwens, R. J., Illingworth, G. D., Labbe, I., & Stefanon, M.
    2018, ApJ, 855, 105
Oesch, P. A., Brammer, G., van Dokkum, P. G., et al. 2016, ApJ, 819, 129
Oesch, P. A., Dokkum, P. G. v., Illingworth, G. D., et al. 2015, ApJL, 804, L30
Oguri, M. 2010, glafic: Software Package for Analyzing Gravitational Lensing,
    Astrophysics Source Code Library, record, ascl:1010.012
Oke, J. B., & Gunn, J. E. 1983, ApJ, 266, 713
Ono, Y., Ouchi, M., Curtis-Lake, E., et al. 2013, ApJ, 777, 155
Pacucci, F., Dayal, P., Harikane, Y., Inoue, A. K., & Loeb, A. 2022, MNRAS,
    514, L6
Peng, C. Y., Ho, L. C., Impey, C. D., & Rix, H.-W. 2002, AJ, 124, 266
Pontoppidan, K., Blome, C., Braun, H., et al. 2022, ApJL, 936, L14
Rayner, J. T., Toomey, D. W., Onaka, P. M., et al. 2003, PASP, 115, 362
Rigby, J., Perrin, M., McElwain, M., et al. 2022, arXiv:2207.05632
Roberts-Borsani, G., Morishita, T., Treu, T., Leethochawalit, N., & Trenti, M.
    2022a, ApJ, 927, 236
Roberts-Borsani, G., Treu, T., Mason, C., et al. 2022b, arXiv:2207.01629
Roberts-Borsani, G. W., Ellis, R. S., & Laporte, N. 2020, MNRAS, 497, 3440
Robertson, B. E., Ellis, R. S., Furlanetto, S. R., & Dunlop, J. S. 2015, ApJL,
    802, L19
Salmon, B., Coe, D., Bradley, L., et al. 2020, ApJ, 889, 189
Schaerer, D., Marques-Chaves, R., Oesch, P., et al. 2022, A&A, 665, L4
Schlawin, E., Leisenring, J., McElwain, M. W., et al. 2021, AJ, 161, 115
Sheth, R. K., Mo, H. J., & Tormen, G. 2001, MNRAS, 323, 1
Shibuya, T., Kashikawa, N., Ota, K., et al. 2012, ApJ, 752, 114
Skelton, R. E., Whitaker, K. E., Momcheva, I. G., et al. 2014, ApJS, 214, 24
Stark, D. P., Walth, G., Charlot, S., et al. 2015, MNRAS, 454, 1393
Stefanon, M., Labbe, I., Bouwens, R. J., et al. 2017, ApJ, 851, 43
Steidel, C. C., Giavalisco, M., Dickinson, M., & Adelberger, K. L. 1996, AJ,
    112, 352
Stiavelli, M., & Trenti, M. 2010, ApJL, 716, L190
Tacchella, S., Johnson, B. D., Robertson, B. E., et al. 2022, arXiv:2208.03281
Trenti, M., Bradley, L. D., Stiavelli, M., et al. 2012, ApJ, 746, 55
Treu, T., Roberts-Borsani, G., Bradac, M., et al. 2022, ApJ, 935, 110
van der Wel, A., Franx, M., van Dokkum, P. G., et al. 2014, ApJ, 788, 28
Vanzella, E., Pentericci, L., Fontana, A., et al. 2011, ApJL, 730, L35
Wang, X., Cheng, C., Ge, J., et al. 2022, arXiv:2212.04476
Whitaker, K. E., Franx, M., Leja, J., et al. 2014, ApJ, 795, 104
Williams, C. C., Curtis-Lake, E., Hainline, K. N., et al. 2018, ApJS, 236, 33
Williams, H., Kelly, P. L., Chen, W., et al. 2022, arXiv:2210.15699
Yamanaka, S., & Yamada, T. 2019, PASJ, 71, 51
Yan, H., Ma, Z., Ling, C., et al. 2023, ApJL, 942, L9
Yang, L., Morishita, T., Leethochawalit, N., et al. 2022, ApJL, 938, L17